Analysing spectra of X-ray active black hole binaries using empirical models

Bachelorarbeit aus der Physik

Vorgelegt von

David Horn

am **09.09.2022**

Dr. Karl Remeis-Sternwarte Bamberg

Friedrich-Alexander-Universität Erlangen-Nürnberg

Betreuer: **Prof. Dr. Jörn Wilms**

Abstract

In this work data from X-ray active black hole binaries was fitted using various empirical models, this data comes from RXTE observations using the PCA detector and was analysed using the software tool ISIS. The sources chosen for this analysis are LMC X-1, LMC X-3, GX 339−4, and Cygnus X-1, as they show a strong X-ray activity and promising behavior in spectral variability for this kind of analysis. In addition to fitting the data exclusively using empirical models, hardness intensity diagrams for all of the sources were created showing the behavior regarding their spectral states. The scope of this work was to create a detector and model independent baseline for the behavior of X-ray active black binaries, which ideally can later be used to determine which of the various currently available physical models gives the best and most general description for these kind of objects.

Contents

1 Introduction

For long time now scientists have taken an interest in X-ray active objects detectable in the universe (Tananbaum et al. 1972). And also for a long time now they have determined that some of these objects are black holes (Bolton 1972). In this work I will be focusing on X-ray active binary systems containing a black hole. Here only systems containing one black hole and one companion star will be considered, as there are numerous of these objects detectable via satellites (Tetarenko et al. 2016). In particular I will be analysing data of LMC X-1, LMC X-3, GX 399−4, and Cygnus X-1.
The thing that makes these objects especially interesting are the rather short times (months) with which their spectral states can change (Wilms et al. 2001; Kong et al. 2002; Böck et al. 2011). Although we are able to see this variability in the satellite data, as will be shown in section 5, this data itself does not tell us how the binary system is structured or how it will behave in the future.
To get such information about the source one usually fits a model to the data. This model can be one of two types, the first one being a physical model and the other one being a empirical model. The first kind is constructed by assuming the source to have a certain physical structure and behavior. By doing so one can model various qualities of the source like for example its spin (see, for example García et al. 2014). But one has to be careful when constructing a model like this as it is possible to make assumptions that are not general enough leading to a model only applicable to a certain or only few sources.
The second approach to fit models to satellite data of black hole binaries is to use empirical models (for example a power law model), that is models that only fit the shape of the observed spectrum, not making broad assumptions about the source (see, for example Wilms, J. et al. 2006). These models are especially useful to get information about the luminosity of the source in question, which is also what they will mainly be used for in this work. In section 4 I will show how several empirical models were fit to the data.
To find the most general physical model one could take every physical model and apply it to every source, but since physical models often are slightly more complicated than empirical ones (compare for example the model described in García et al. (2014) and a power law model) this would be quite an enormous undertaking. Another approach to this problem is to apply empirical models to every source and ideally find a general behavior of black hole binaries. If such a behavior can be determined one could in the next step check which physical model (or models) also describes this behavior and thus find the most general physical model or find out which physical models are equivalent in describing the general behavior of black hole binaries. This would shorten the process of finding the most general physical model, as one would no longer have to apply physical models to actual satellite data.
This thesis will build the basis of this process by applying multiple empirical models to the previously mentioned sources and analysing the emerging results. The usage of physical models will not be touched on in this work. The results of this groundwork are presented in section 5. The following two sections will contain a brief introduction of the

general structure of black hole binaries (section 2) followed by some information about the observations used in this work and the objects themselves (section 3).

2 X-ray Binaries

Before introducing the specific sources analysed in this work and showing the results, I want to give an introduction into the kind of objects we are working with. Throughout this whole work I focused on binary systems containing one companion star and one compact object. The compact object contained in all of the considered sources is thought to be a black hole (Tetarenko et al. 2016).
Before going into details about the general structure of these kind of binary systems I want to introduce the concept of Roche potentials and Roche lobes, as later this is important to understand the classification and mass transfer of binary systems consisting of a black hole and a companion star.

2.1 Roche Potential and Roche Lobes

Imagine two masses m and M with $M \geq m$, orbiting each other on circular orbits with a constant frequency. Applying the restricted three-body problem to this situation one finds five points in space where all forces in this system cancel out, as discussed in Frnka (2010). These points are called Lagrange points and are usually labeled as L_1–L_5. The potential caused by these masses is given by

$$\Phi = -\frac{GM}{r_1} - \frac{Gm}{r_2} - \frac{\omega^2}{2}\left[\left(x - \frac{m}{(M+m)}\right)^2 + y^2\right] \tag{2.1}$$

where $r_1 = (x^2 + y^2 + z^2)^{1/2}$, and $r_2 = [(x-1)^2 + y^2 + z^2]^{1/2}$ and ω is the frequency with which the masses orbit each other (Hilditch 2001, equation 4.46). As an example Fig. 1 shows how the Lagrange points are positioned (for an artificial example constellation of no further significance). Furthermore this figure shows the equipotential lines of each Lagrange point, that is the lines along which the potential has the same value as at the corresponding Lagrange point. The equipotential lines for L_4 and L_5 were rescaled to have lower potential values, otherwise they would only appear as hardly visible points, since they are maxima of the potential. The potential in question here is also referred to as the Roche potential (Hilditch 2001). An important characteristic of this potential are the so called Roche-lobes, material that is within this region is gravitationally bound to the star/ black hole. Each object in the binary system has a Roche-lobe, they meet at the first Lagrangian point L_1, they are marked as red, “infinity-symbol-shaped” lines in Fig. 1. Keep in mind that this plot only shows a slice through the potential along one coordinate axis. In reality the Roche lobes are cross sections of three dimensional volumes around the objects of the binary systems. These volumes are often referred to as Roche volumes. Furthermore I also want to mention that this plot was made by using the python package PyAstronomy and by altering the given code example for Roche lobe

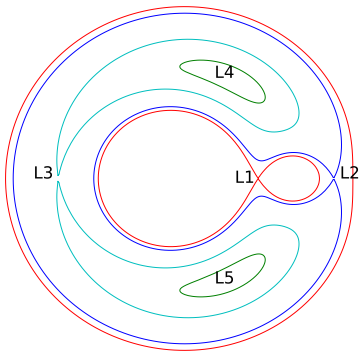

Figure 1: Example of equipotential lines, Roche lobes shown on the inside in red, circling L_1. The equipotential lines of L_4 and L_5 are scaled by a constant factor, as otherwise they would only appear as points. The star/ black hole would each be situated at the center of one of the lobes, with the black hole occupying the smaller, right lobe.

plots[1]. The importance of the Roche lobes and subsequently the Roche volume will be made clear in the following section.

2.2 General Structure

In general binary star systems consist, as the name already suggests, of two objects, these could just be stars, but also other stellar bodies like white dwarfs, neutron stars or black holes. Sometimes one of the two bodies is a compact object like a black hole or a neutron star and the other one is a companion star (Hilditch 2001). Here I want to focus on binary systems consisting of a black hole as the compact object and a star as a companion. From here on these binary black hole-companion star systems will just be referred to as black hole binaries.
Next we want to be able to classify these black hole binaries, this is often done via the mass of the companion star and therefore also via the way they transfere matter to the compact object, as will be explained shortly. The first kind are the so called Low Mass X-ray Binaries (*LMXBs*) with a mass $m \lesssim 10\,\mathrm{M}_\odot$. The other kind of objects are called High Mass X-ray Binaries or in short *HMXBs* and have a mass $m \gtrsim 10\,\mathrm{M}_\odot$.
As discussed in the previous section the two stellar objects form a Roche potential and are each centered in their respective Roche Lobe. The size of these Roche lobes is dependent on the mass ratio $q = m/M$ of the two objects, so it also possible to have stars that are bigger than their Roche lobe, which is often the case for old low mass stars. This of course leads to mass transfer from one star (here the companion star) to the other object,

[1] https://pyastronomy.readthedocs.io/en/latest/pyaslDoc/aslDoc/aslExt_1Doc/roche.html

since the star that is bigger than its Roche lobe now crosses the first Lagrange point L_1. This process is called Roche Lobe overflow (Hilditch 2001). LMXBs usually show this kind of behavior and often consist of a black hole and a late type companion star, i.e., a star that is so old that it grew beyond its Roche lobe (Grinberg 2013). HMXBs usually consist of a high mass companion that does not necessarily fill its Roche lobe (but is not forbidden to do so). Here mass transfer can not only happen through Roche Lobe overflow but also via stellar winds from the companion star, which usually is an early type star. The classification introduced here follows the one given in Grinberg (2013)
After "escaping" the companion star towards the compact object, the escaped matter does not just fall into the black hole in a straight line. As the binary system keeps on rotating and as the matter starts moving towards the black hole an accretion disk forms, since the matter slowly spirals towards the black hole (Carroll & Ostlie 2017).
Since we can measure radiation coming from these compact objects there must be a process creating (X-ray)photons. And actually there are multiple such processes. First radiation is produced by matter falling towards the compact object. This will be explained via the following example:
Imagine a star of mass M and radius R and another small test mass m resting at infinity. The initial mechanical energy of this small mass is given by

$$E = K + U = 0 \tag{2.2}$$

where K is its kinetic energy and U is its potential energy. If the object were to radially fall onto the star it would reach a kinetic energy of

$$K = -U = G \cdot \frac{M \cdot m}{R} \tag{2.3}$$

since it has to obey conservation of energy. Upon impact this kinetic energy is converted into heat and radiation, which then can be measured by an observer.
Of course this situation is slightly different from a binary system consisting of a black hole and a companion star, but it helps us to understand why matter crossing L_1 and falling towards the black hole causes radiation. Just like in the example above matter in the binary system falls towards a heavy object, which in our case just happens to be a black hole. But here instead of radially falling towards the black hole the matter has some angular momentum, since previously it was moving along the rotation of the companion star. Due to this angular momentum the infalling matter "misses" the compact object when falling towards it and swings back around it forming a loop shaped path. If enough matter crosses L_1, a lot of particles move along such loop and eventually collide into one another, this process is depicted in Fig. 2. These collisions lead to randomization in the movements of the particles, which then again leads to the formation of circular orbits around the black hole (Wilms 2022, chapter 3). If enough particles form these circular orbits we call this an accretion disk. After the formation of this accretion disk particles will continue to collide with one another, transferring their angular momentum to their collision partner and moving further inwards towards the black hole. These collisions lead to disordered motion and to thermalization (Wilms 2022). Since we assume the disk

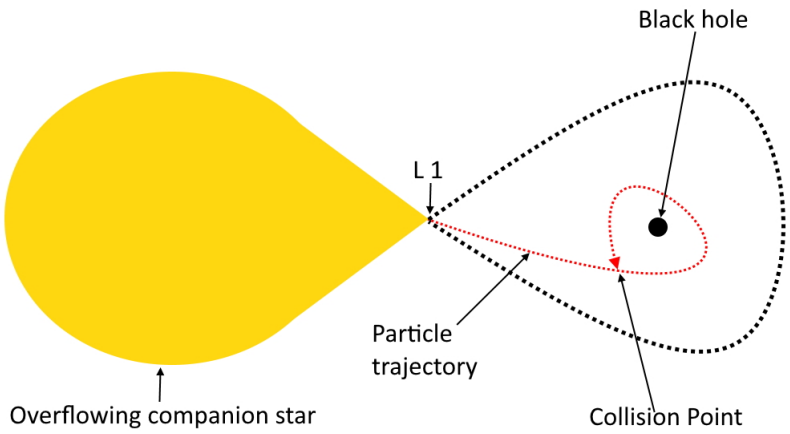

Figure 2: Schematic structure of Roche overflow through the L_1 Lagrange point (figure inspired by Lubow & Shu (1975)).

to be optically thick (Wilms 2022), we can assume the spectrum emitted by the disk at a given radius to be given by a black body, assigning a wavelength and therefore also an energy to the temperature of the disk.
But this is not the only source of radiation in binary black hole systems. In addition to the accretion disk itself radiating, there is also another place in black hole binaries producing X-ray photons. This place is situated close to the black hole itself and according to (Sunyaev & Titarchuk 1985, and references therein) consists of a hot plasma producing photons via Comptonization. This radiation appears as the hard (high energy) part of the black hole binary's spectrum and appears to have the shape of a power law spectrum with an exponential cutoff (Mondal et al. 2014).
Since this Comptonized radiation not only travels directly towards the observer but in all directions away from where it is produced, this also can lead to another aspect of the X-ray spectrum. Hard radiation coming from close to the black hole also hits the accretion disk. This can cause ionization of the components of the disk, which then in turn can lead to emission lines in the observed spectra. These emission lines are subject of Mondal et al. (2021), where it is mentioned that the Fe-emission line is often observed in black hole binaries. This was also already previously discussed in Barr et al. (1985). As we will see later on in section 5, the spectra analysed in this work also sometimes happen to contain such an emission line between 6 keV and 8 keV.

2.3 Spectral Variability

As previously suggested black hole binaries can show a change in their spectra. This change can express itself in different ways, for example in the total amount of detectable

photons emitted by the source, the width and position of the iron line or the slope of the spectrum towards higher energies. All of these changes will be visible in the spectra shown later on in section 5.
To classify this variability-behavior we distinguish different states of the black hole binary, namely hard and soft states. These correspond to different behaviors in the black body part of the spectrum, i.e., the part corresponding to radiation from the accretion disk and also to the slope of the spectrum. Black hole binaries in a hard state have a weak black body spectrum, therefore the ratio of high energy (or *hard*) photons to low energy (or *soft*) photons is higher. Hence the name hard state. For soft state black hole binaries the situation is reversed and the black body part of the spectrum corresponding to the disk radiation is more pronounced than the high energy part of the spectrum. This separation in high and low energies for these kinds of objects can mean a distinction between energies below and above 5 keV, but this boundary can differ depending on the specific source, as it is only a way of dividing the spectrum into two parts, with the components of each part behaving in similar ways respectively (see, for example Tetarenko et al. 2016, Fig. 4 ff.).
To classify black hole binaries via their spectral variability one introduces the notion of persistent and transient black hole binaries. The difference is the amount of time the source appears to be emitting a high amount radiation, i.e., the amount of time in which the black hole accretes a lot of matter. Transient sources spend most of their time in a dim state and only occasionally have bright outbursts, in contrast to this persistent sources are usually in their bright state and only sometimes show a drop in their accretion rate, i.e., they become fainter due to less matter crossing the Lagrange point. Usually HMXBs are persistent sources, whereas LMXBs usually are transient sources. More details about this classification and the behavior of the respective binary black holes can be found in Tetarenko et al. (2016).

2.4 Hardness Intensity Diagrams

The just explained variability can be nicely shown in so called Hardness Intensity Diagrams (*HID*s). Figure 3 shows the rough shape one ideally would like to see in a HID, it also shows which regions in the HID correspond to hard and soft states respectively. It should be noted that not every source will result in a HID of this shape, it might also be that the source only fills out part of this q-shape, which then could for example just look like a horizontal line in the HID, as we will see later on in section 5. Furthermore these diagrams show the intensity of the source plotted over its hardness h, which is the ratio of the sources intensities in different energy bands, it could for example be defined like this: $h = \frac{\text{Intensity at } 5.0\text{–}10.0\,\text{keV}}{\text{Intensity at } 1.5\text{–}5.0\,\text{keV}}$, which is sometimes referred to as the simple ratio (Park et al. 2006). One more important thing to note here is that the energy ranges of this ratio are not fixed, one can choose them almost arbitrarily. Depending on the source, different energy bands could result in “better” and more meaningful HIDs. More about hardness ratios and their computation can be found in (Park et al. 2006, and the references therein).
Also there are different kinds of HIDs. One could for example use the flux density of the

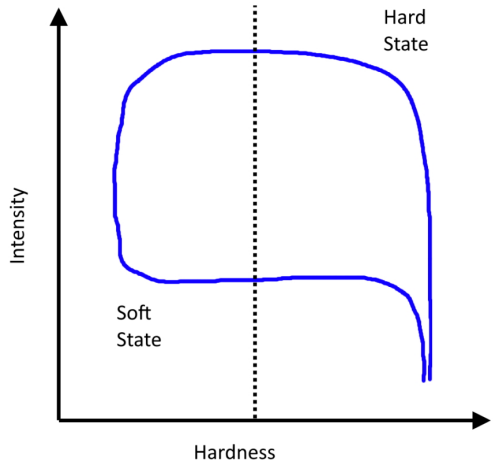

Figure 3: Simplified general shape of a HID diagram, the system could for example start at the bottom right corner and make its way anti clockwise around the diagram during its transition (see Tetarenko et al. 2016, Fig. 1).

source as a measure of intensity, but it is also possible to make a luminosity-dependent HID, as these two quantities are related via the inverse square law

$$L = 4\pi \cdot r^2 \cdot F \tag{2.4}$$

where L is the luminosity, r the distance to the source and F denotes its flux-density, furthermore this formula assumes the star to be a point-like light source. To make this a bit more clear the flux-density of a source is the amount of energy coming from the source passing through an area per amount of time, thus its unit of course is $\mathrm{W\,m^{-2}}$. So by knowing one of these measures one can infer the other. But unfortunately from our satellite data we get neither of these values directly, but have to calculate then from the measured rate, that is the amount of photons measured per time per energy. And since the satellite-detector can resolve wavelength (up to a certain point) and therefore also photon energies (Jahoda et al. 2006), it is possible to measure how many photons of a certain energy hit the detector in a certain time interval. Furthermore one has to take into account background noise and substract it from the total signal. Adding to this the knowledge about the size of the detector chip one can calculate the flux and therefore also the luminosity of a source. An additional step that is sometimes done is calculating the flux of a source as if it were at a distance of 1 kpc, this allows for an easier and better comparison between sources. This recalculation can easily be done by simply using $r = 1\,\mathrm{kpc}$ in equation 2.4 instead of the actual distance of the source of radiation. Additionally there are multiple other ways of making HIDs, for example one could also use the fractional difference, as defined in Park et al. (2006), as a hardness measure.
First and foremost HIDs let us understand how a source changes its total intensity

depending on its hardness, i.e., if it is bright or dim when it is in its hard or soft state respectively. This of course is an indication for how much matter is being accreted at a certain time, as more matter falling inward would also result in a higher intensity. But all of this is only one part of the HID, in addition to the intensity it also shows the hardness ratio of the light source, this ratio tells us which parts of the objects spectrum are bright and which are dim.

3 Observations

For this thesis observations of four different X-ray sources were used. These sources are LMC X-1 and LMC X-2, as well as GX 339−4, and Cygnus X-1. Each of these objects is believed to be a X-ray active black hole binary (Tetarenko et al. 2016), therefore it is justified to apply similar models to all four sources when fitting. The details concerning the fitting to the observation data are given in section 4.
All observations were performed using the **R**ossi **X**-Ray **T**iming **E**xplorer (**RXTE**). More precisely the so called **P**roportional **C**ounter **A**rray (**PCA**) onboard of the RXTE was used for pointed observations, it consists of five proportional counters and is most sensitive from 2–60 keV. More about the PCA and the other instruments aboard the RXTE can be found on the HEASARC website[2]. Technical details about the PCA and its calibration can be found in Jahoda et al. (1996) and Jahoda et al. (2006).
Not all of the here analysed objects were observed for the same amount of time or during the same period of time, their respective total exposure times can be seen in Table 1, their observation times, as well as the respective exposure times of each observation are also shown in Fig. 4. In addition to the total exposure times Tab. 1 also shows the assumed distances of each object in kpc (Hynes et al. 2004; Xiang et al. 2011; Pietrzyński et al. 2019). For the two LMC sources I used the distance of the LMC itself. In the following some more details about the observations of each object and the objects themselves are given.

3.1 LMC X-1

LMC X-1 is a persistent binary system consisting of a black hole and a companion star. It is situated, as the name already suggests, in the Large Magellanic Cloud (LMC). LMC X-1 is a High-Mass X-ray binary and also the brightest X-ray source in the LMC (Hyde et al.

[2] https://heasarc.gsfc.nasa.gov/docs/xte/xtegof.html

Table 1: Total exposure time for each source given in ks; Distance of each source given in kpc.

	LMC X-1	LMC X-3	GX 339−4	Cygnus X-1
Total Exposure [ks]	924	2447	2427	4162
Distance [kpc]	49.59	49.59	6	1.81

2017; Tetarenko et al. 2016). The observation starting times and corresponding exposure times are shown in Fig. 4. As is visible by this figure most observations happened roughly between the years 2007 and 2010 and were shorter than one hour. Something important to note about this source is the fact that the satellite was not perfectly pointed at the source for all observations. This can be seen in Fig. 5a and 5b. The declination and right ascension values should be the same or at least very similar for all observations. As an example of what it should look like Fig. 5 shows the satellites right ascension during the GX 339–4 observations. In total 439 observations of LMC X-1 were used in this thesis. The N_{H}-value for this source was taken from Hanke et al. (2010) to be in the range $1.0–1.3 \times 10^{22}\,\mathrm{cm}^{-2}$.

3.2 LMC X-3

Similar to LMC X-1, LMC X-3 is also situated in the Large Magellanic Cloud, but it can be classified as a strongly variable source. This is due to the fact that it appears to be mostly fed by Roche lobe overflow (Tetarenko et al. 2016, 2.2.3). Although this seems to be its main way of mass transfer it also can transfer mass via stellar winds and is therefore close to being a persistent source (Steiner et al. 2014). For this reason some sources also classify LMC X-3 as a persistent HMXB (Tetarenko et al. 2016). Additionally LMC X-3 is also a high-mass X-ray binary with a black hole as its compact object. The observation and exposure times for LMC X-3 are also shown in Fig. 4. As can be seen in this figure, there are more observations of LMC X-3 than of LMC X-1, in particular I used 1101 LMC X-3 observations for this work, which resulted in an total exposure time of 28.32 d. The upper limit of $0.08 \times 10^{22}\,\mathrm{cm}^{-2}$ for the N_{H}-value of this source was taken from Page et al. (2003).

3.3 GX 339–4

In contrast to the two previous sources this one is not a high- but a low-mass binary, which also consists of a black hole and a companion star “feeding” the compact object (Zdziarski et al. 2004). In Tetarenko et al. (2016) this source is classified as a transient X-ray binary. Also it is not situated in the LMC but it is a galactic X-ray source in the Ara-constellation, at a distance of $\approx 6\,\mathrm{kpc}$ (Hynes et al. 2004). Details about its coordinates can be found using the SIMBAD Astronomical Database[3]. This source has already been extensively studied, as it was also already discovered in 1972 (Tetarenko et al. 2016, 2.2.24). Again the exposure times of the RXTE-observations used in this thesis can be seen in Fig. 4.

3.4 Cygnus X-1

Finally I come to the last source examined in this thesis: Cygnus X-1, which is located in the cygnus-constellation of the milky way, is one of the brightest X-ray sources in the observable universe (Tetarenko et al. 2016, 2.2.71) and also the first confirmed X-ray

[3] https://simbad.unistra.fr/simbad/

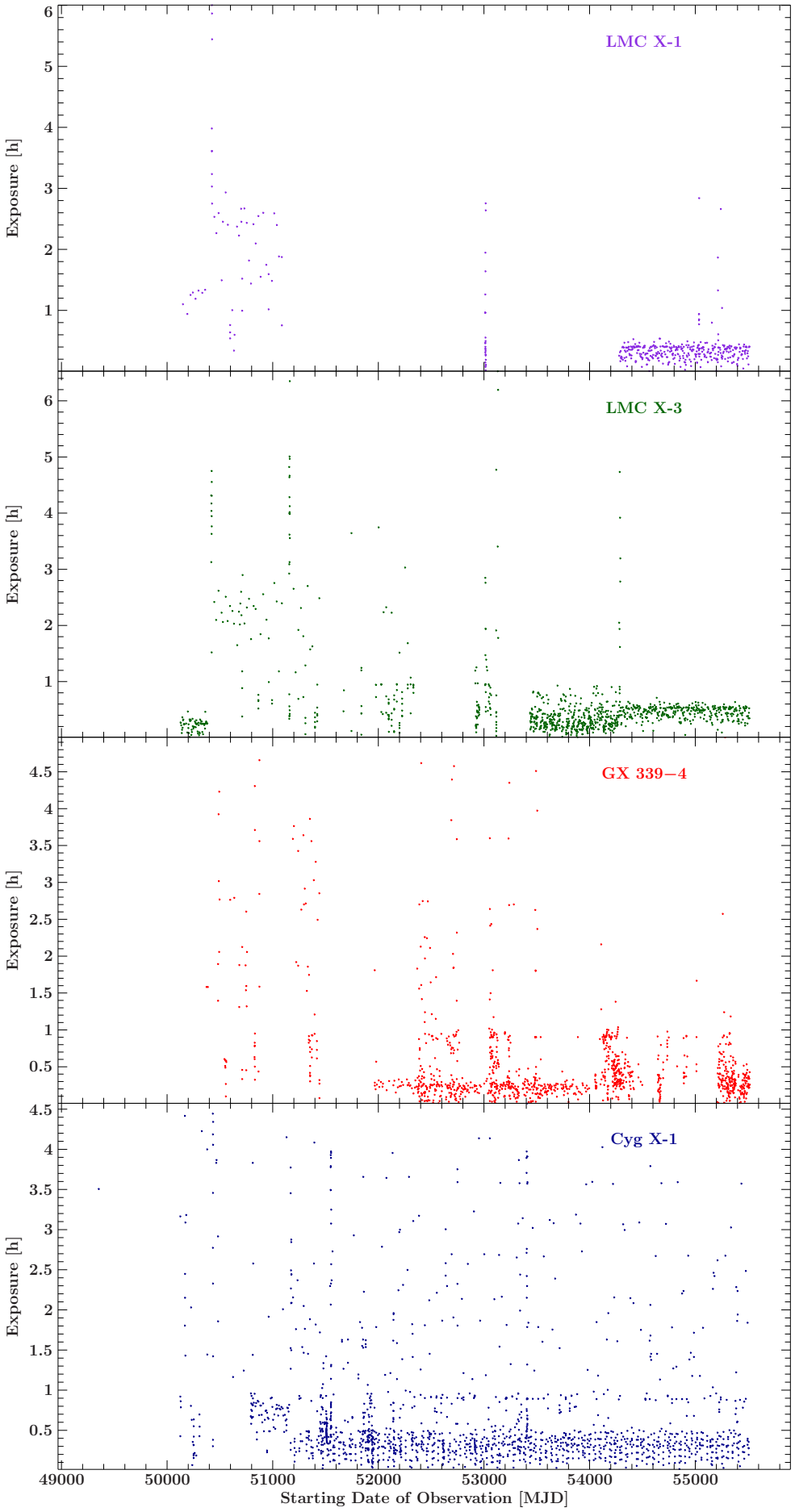

Figure 4: Exposure times in hours of each studied source as a function of time.

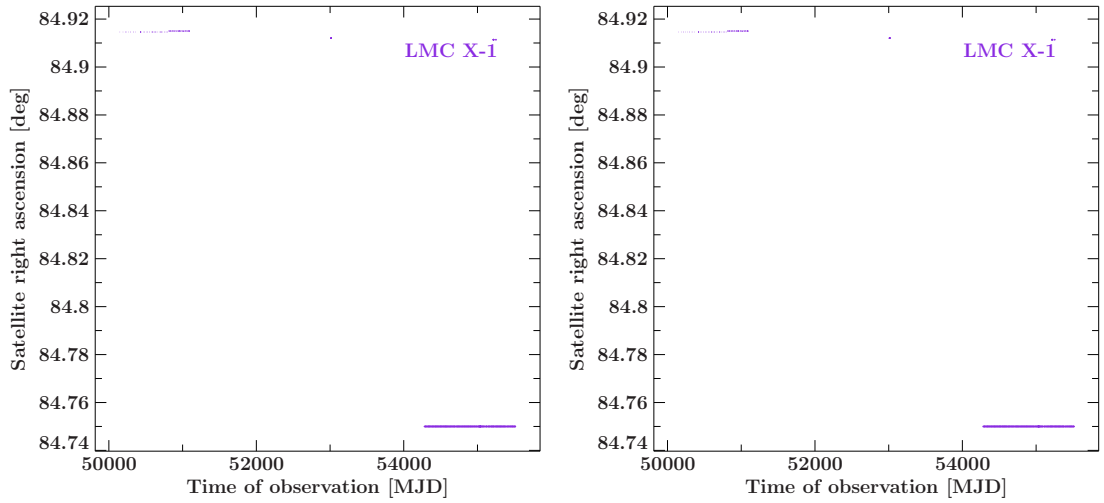

(a) Right ascension of the satellite for each LMC X-1 observation.

(b) Declination of RXTE for each LMC X-1 observation.

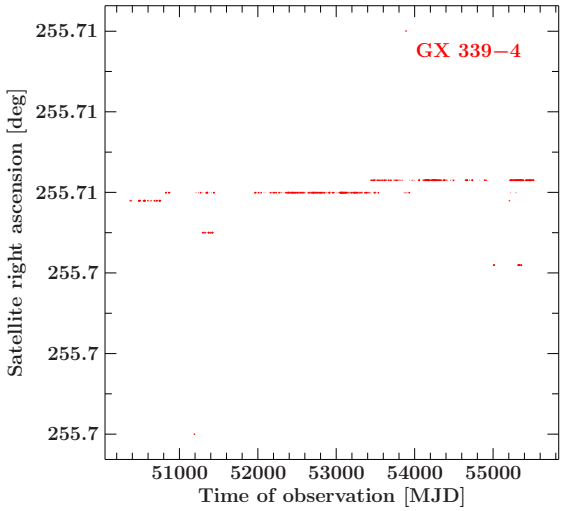

Figure 5: Right ascension of the satellite for all GX 339−4 observations.

binary (Bolton 1972; Tananbaum et al. 1972). As can be seen from Fig. 4 Cygnus X-1 is the object with the most observations and highest exposure time in this work. This and the fact that it exhibits a high count rate (partially due to its low distance of $\approx 1.81\,\mathrm{kpc}$ (Xiang et al. 2011) from earth) will likely result in generally better fits. Especially interesting about this source is the high mass of its compact object, with $21.2\,M_\odot$ Cygnus X-1 by far contains the most massive black hole within the four sources examined in this thesis (Miller-Jones et al. 2021).

4 Fitting

For fitting a model to the data multiple empirical models have been used. Following this the best fits and therefore also the best models were determined from the χ^2_{red}-value, which will be explained in detail in section 4.3. Spectral fitting was necessary for this work, as the energy fluxes needed for the HIDs can be calculated from a fit model. But before going into detail about the fitting procedure itself, the software, as well a models used for fitting will be introduced and explained.

4.1 Fitting Software

Throughout this thesis a X-ray analysis software tool called the **I**nteractive **S**pectral **I**nterpretation **S**ystem or in short **ISIS** was used. This software tool was developed at MIT (Houck & Denicola 2000). All fits shown in this thesis were generated using ISIS version 1.6.2-48. Additionally to the ISIS-tool a collection of ISIS-scripts was used, which was provided by the ECAP/ the Remeis Observatory and MIT. More about this collection of scripts can be found on the corresponding website[4]. In addition to the Isis software and the provided scripts I also made use of a few additional ISIS-scripts, some of which were provided by Jörn Wilms. These scripts as well as a multitude of self written scripts were used to be able to efficiently fit models to the data and to plot and analyse the results.

4.2 Empirical Models

First I want to make clear why I only used empirical models, i.e., models that only make few to no assumptions about the object and only fit the shape of the spectrum, rather than assuming any physical values like the mass of the object for example. As previously explained this work is the groundwork for being able to find the most general physical model, but for this we first need to have a baseline for what qualifies as a “good” physical model. And as a measure for this “goodness” I first have to fit empirical models to the data without making broad assumptions about the objects. From these empirical fits one can then determine the best one and use it to make a HID. This HID would then be independent of the detector that was used for the observation, since only the actual empirical behavior of the source was used to make this HID. To determine the

[4] http://www.sternwarte.uni-erlangen.de/isis/

best physical model one would have to compare the HIDs produced by these models with the empirical-HID, if a physical model shows the same behavior as the empirical ones the model can be accepted otherwise one has to reject this model as a general one.
Although this procedure could potentially determine the most general physical model it is not without flaws. This whole procedure hinges on the assumption that all black hole binaries show a behavior that can be classified using HIDs. If this is not the case the HID also does not give us any useful information about the generality of a physical model. The flaws of this empirical model approach will not be further explored in this work, as one would need to use a higher number of different sources and to check for the applicability of physical models, which would exceed the scope of this work.
Before going into the fitting procedure itself, the ISIS-models used in this work will be introduced:
First all of the fits included an absorption part, which was implemented via the so called `tbabs` model. This model allows the user to vary the equivalent hydrogen column and thereby model the absorption caused by the interstellar medium or the gas within the accretion disk (Wilms et al. 2000). Of course this model was included in every fit, as it is reasonable to assume that at least some absorption happens in between the black hole binary and the satellite.
The following models will be introduced by themselves, but keep in mind that in practice one almost always uses some combination of these models.
The first of these models is called the `powerlaw`-model, as the name already suggests this models a power law according to:

$$A(E) = K \cdot E^{-\Gamma} \tag{4.1}$$

where Γ denotes the dimensionless photon index and K is the norm of the model, it characterises the amount of photons per keV per cm^2 per s at an energy of 1 keV. Lastly E of course is the energy, which here is the input variable of the model, it is also measured in keV.
Many of the fits also include a `diskbb`-model, which stands for disk black body. This `diskbb`-model fits a black body spectrum to the data, the peak of this black body is set to be at energies < 1.5 keV. This represents the soft (low energy) component of a spectrum. More details about the disk black body model can be found in Mitsuda et al. (1984) and Makishima et al. (1986). Figure 6 shows both the power law and the disk black body component of a fit, it also shows the data and the complete fit itself. Fig. 6a shows the folded and Fig. 6b the unfolded model, folded meaning it was folded through the response matrix. The power law component in Fig. 6b is a straight line, since it is plotted with two logarithmic axes. Before going into the slightly more complicated models the gaussian absorption/emission model (`egauss`) will be introduced, which here models a gaussian iron emission line. The limits for the center of this line were set to be between 6 keV and 8 keV. The energy range in which this line lies has to be restricted to this band, otherwise it could more easily interfere with other model components. Additionally to restricting the range of the center of the gaussian emission line, I also restricted the width of the line to 0.3 keV in case of the LMC sources and 0.5 keV for the other two systems, again to stop the line from interfering with the disk black body component. Figure 7 shows

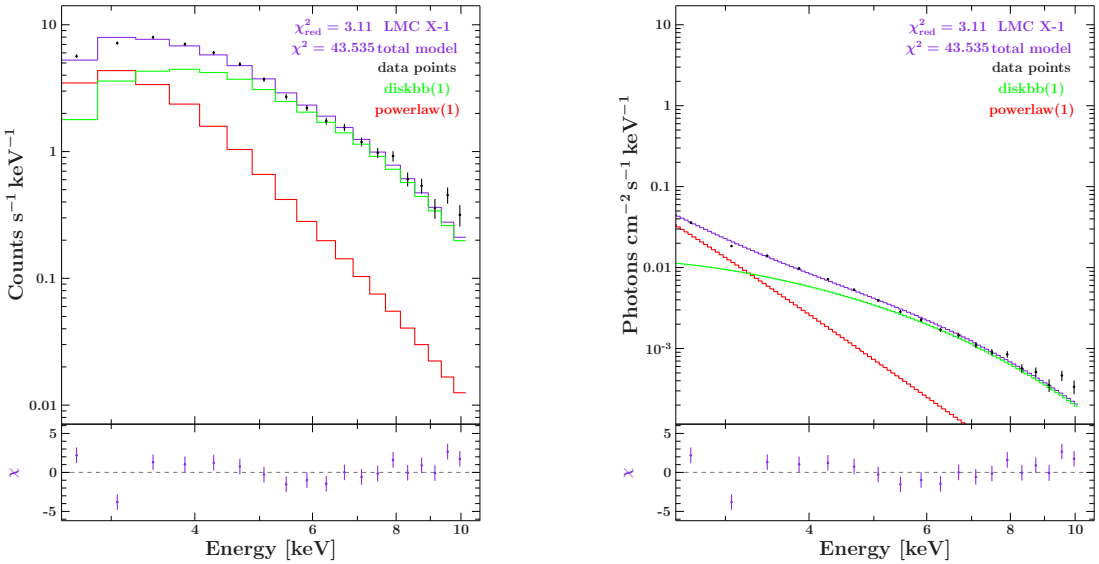

(a) Model folded through response matrix.

(b) Unfolded model.

Figure 6: Fitted spectrum of LMC X-1 with individual fit-components, total fit and data points. Here every model component is also multiplied with the `tbabs` model.

this (blue line) as a component of a model consisting of multiple other components.
The first of these other components is the `highecut`-model, which is an exponential energy model that only contributes if the energy is above a certain threshold, i.e., above the so called cutoff energy. This model is described by:

$$A(E) = \begin{cases} \exp((E_c - E)/E_f) & E \geq E_c \\ 1.0 & E \leq E_c \end{cases} \tag{4.2}$$

Here E_c is the cutoff energy, E is the input variable and E_f is the so called folding energy. All of these parameters are measured in keV.
The last model used in this work is called the `bknpower`-model, which stands for broken power model. Here the models contribution is given by:

$$A(E) = \begin{cases} K \cdot E^{-\Gamma_1} & E \leq E_{\text{Break}} \\ K \cdot E_{\text{Break}}^{\Gamma_2 - \Gamma_1} \cdot (E/1\,\text{keV})^{\Gamma_2} & E > E_{\text{Break}} \end{cases} \tag{4.3}$$

where the model basically gives two different power laws, depending on whether the input energy E is below or above the breaking energy E_{Break}. The two Γ-parameters are two photon indices characterising the model as shown in equation 4.3. Similar to the basic power law model here again K is the norm factor of this model. Also as before Fig. 7 shows an example spectrum with its corresponding fit and the individual model components of this fit. This figure also shows both the folded and unfolded model. The folding through the response matrix is the reason why Fig. 7a shows a Compton tail

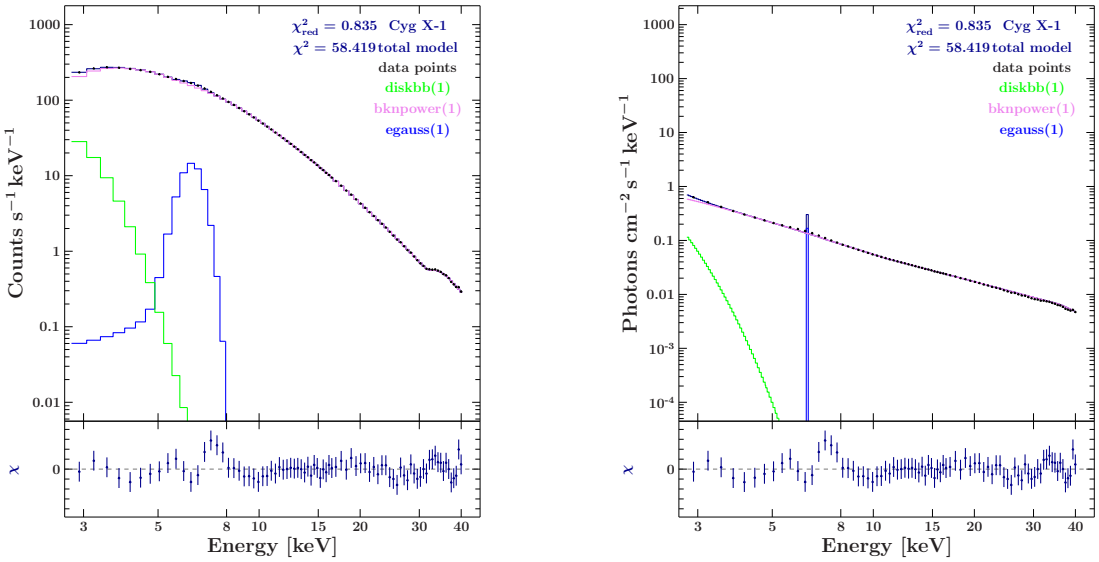

(a) Model folded through response matrix.

(b) Unfolded model.

Figure 7: Fitted spectrum of Cygnus X-1 with individual fit-components, total fit and data points. Again here every model component is also multiplied with the `tbabs` model, additionally the broken power law component is also multiplied with the previously introduced high energy cut-off model.

at the lower energy end of the gaussian emission line component. One more thing to note here is that the high energy cut-off model was always used in combination with the broken power law model, as it is a multiplicative model. In contrast all other models, except for the absorption model, are additive.
These last two models were only used for fitting data of GX 339–4 and Cygnus X-1. Since the LMC sources show low count rates at energies above 10 keV it makes little sense to use a model with a breaking energy around this exact mark, as it would for example be the case for the high energy cut-off model. So a total fit model for GX 339–4 or Cygnus X-1 could for example look like this: `tbabs*(diskbb+highecut*bknpower+egauss)`

4.3 Fitting Procedure

One of the first steps in analysing data like this usually consists of extracting and calibrating the data. This was fortunately already done by Jörn Wilms[5]. Thus the next step already was to fit a model to the data. Here I applied an additional systematic error of 1% to all observations. As there were several hundred data sets per source this of course could not be done by hand. To still get a fit for every spectrum I began by fitting a few spectra by hand and using these fits as a starting point for an automatic fitting procedure.

[5] Thank You!

Before going on I want to introduce a measure of goodness for the fits: the reduced chi-squared value χ^2_{red}. This value is calculated via

$$\chi^2_{\text{red}} = \frac{\chi^2}{\#\text{of data bins} - \#\text{of free parameters}} \tag{4.4}$$

where χ^2 is the value one acquires from assuming a chi-squared statistic for the spectrum. Since using a few manual fits as a baseline did not result in particularly good fits, i.e., fits with a $\chi^2_{\text{red}} \approx 1$, I repeated the first step using the acquired fits as a basis. Repeating this process while adjusting the parameters to have physically sensible values, I got rather good fits for Cygnus X-1 and GX 339–4 fulfilling this requirement and only moderately good ones for the two LMC sources (shown in Fig. 8a and 8b are less close to 1 than for the other two sources). The corresponding χ^2_{red} for each source and observation are shown in Fig. 8. It is important to note that each dot in this figure represents the best fit for its corresponding spectrum, this means not all fits in this plot were done using the same model but the one that gave the best χ^2_{red}-value for each observation. As the final step of the fitting procedure the energy flux of the current fit model was calculated using the `energyflux`-function provided by the `isisscripts`-package. The remaining results from this fitting procedure will be shown in the next section.

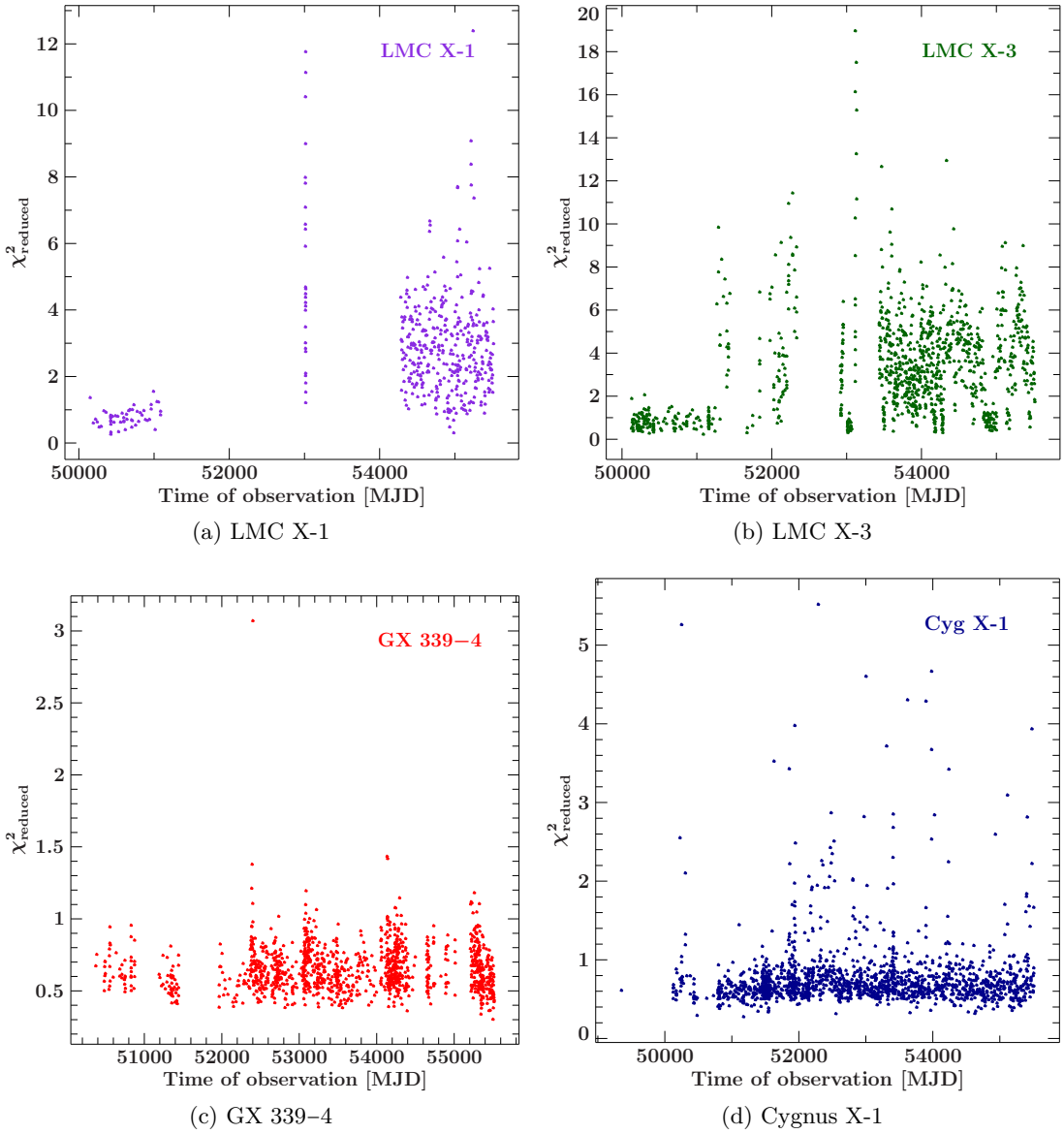

(a) LMC X-1 (b) LMC X-3

(c) GX 339–4 (d) Cygnus X-1

Figure 8: χ^2_{red}-values for each source over the observation time.

5 Results and Discussion

As previously mentioned in section 2.3 not all sources will show the complete q-shape one expects to see in a HID. Both of the LMC sources behave like this, which will be shown in the following subsections. It is important to mention that all luminosity HIDs shown in the following were plotted using the same energy ranges. For the luminosity on the y-axis I used the 2.0–20.0 keV energy band. For the Hardness ratio L_2/L_1 I used the energy bands 1.5–5.0 keV and 5.0–10.0 keV for L_1 and L_2 respectively. One could also use other energy bands, but the interesting behavior of these four sources will already be visible using these energy ranges.
In addition to the respective HIDs I also marked some data points in these HIDs and will show the corresponding spectra, models and model components for these marked data points. Of course I can not show every spectral plot for every source in this thesis as this would make this thesis unnecessarily long, which is why I will only show a few example plots for each object.

5.1 LMC X-1

Figure 9 shows a HID for LMC X-1, the hardness of this sources ranges from ≈ 0.01 to ≈ 0.2, the luminosity stays rather constant and only ranges from $\approx 1 \times 10^{38}$–$2 \times 10^{38}\,\mathrm{erg\,s^{-1}}$. To separate "good" from "bad" fits, data points corresponding to a $\chi^2_{\mathrm{reduced}}$-value > 3.5 are displayed in a lighter shade. As you will see this was done for all sources. As shown in Fig. 10 a)-d) LMC X-1 has a strong disk black body component and a rather constant count rate. This count rate is also the reason for its shape in the HID, as an actual constant count rate would correspond to a perfectly horizontal line in the HID. Here Fig. 10a shows a spectrum of the less soft state of LMC X-1, marked by a more pronounced power law component at high energies ($\approx$ 6–10 keV), the further one moves to the left of the HID the weaker this model component becomes (see Fig. 10a-10c). Also the further we move to the left side of the HID the stronger the disk black body component becomes in the high energy range. As can be seen from Fig 10d this seems not to be the case for spectra at the far left of the HID, where the power law seems to dominate the spectrum. This of course is due to an error in the automatic fitting procedure, the power law photon index was allowed to vary in too big a range and the disk black body temperature in a too narrow range. These "wrong" parameter limits resulted in the fit ending up in a un-physical minimum, which would be just fine for finding the fluxes and luminosities of this observation but clearly does not describe a soft state black hole binary. To fix this issue the parameter limits for these observations were changed to allow for higher temperatures up to 2 keV and for photon indices in the range of 4–9. This resulted in the spectral fit shown in Fig. 11. Furthermore the plots in Fig. 10 also already show that a model including a gaussian emission line did not always result in the best fit for this source. This might be due to the fact that the source is quite dim, resulting in the spectrum often lacking an emission line. As clearly visible by Fig. 9 LMC X-1 does not show the complete q-shape in its HID. Later in section 5.5 it will be shown which part of the q-shape is occupied by LMC X-1.

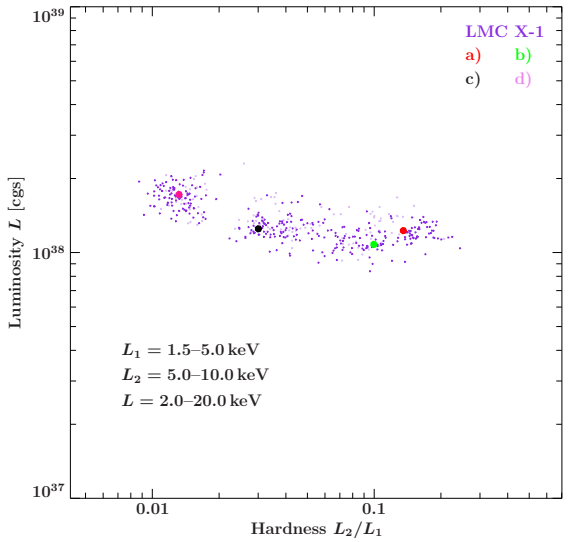

Figure 9: HID of LMC X-1 with marked data points corresponding to spectral plots shown in Fig. 10; data points with $\chi_{\mathrm{reduced}} > 3.5$ shown in a lighter shade.

5.2 LMC X-3

Here we have a similar situation to LMC X-1, the main difference in the HID being the fact, that now we do not see a horizontal line but two diagonal, more or less parallel lines. It should be noted that the data points that clearly do not line up with the diagonal lines could just be due to a especially low count rate in the observation, which considering the already rather low count rate observed in LMC X-3 would mean the data is hardly distinguishable from the background and whatever model we apply for fitting will give ambiguous results. Another aspect not visible in this HID, but in the one shown in Fig. 12b is that the data points on the right diagonal all correspond to earlier observations and the ones on the left diagonal to later observations (in this figure dark point correspond to an early observation date and lighter ones to a later date).

Similar to the previous section Fig. 13 shows spectra from different areas of the HID, in particular from around the ends of the two diagonals. Here the source shows a dominant disk black body model component throughout almost all observations (not just the ones shown in Fig. 12). The behavior of the power law component is similar to the previous source, observations on the right diagonal show a rather flat power law component (Fig. 16a and 16b), whereas the ones on the left diagonal correspond to a very steep power law and thus to a high photon index (Fig. 16c and 16d). Also again the model including an emission line is not always the best fit model, which has the same implications as for LMC X-1. One difference compared to LMC X-1 that is also observable in these spectral plots is LMC X-3's change in count rates. Observations that lie on the top end of one of the diagonals (Fig. 16a and 16c) have a higher count rate than observations that can be found on the low end of the respective diagonal (Fig. 16b and 16d). Since the count rate is directly proportional to the luminosity, this behavior just reflects the diagonal shape

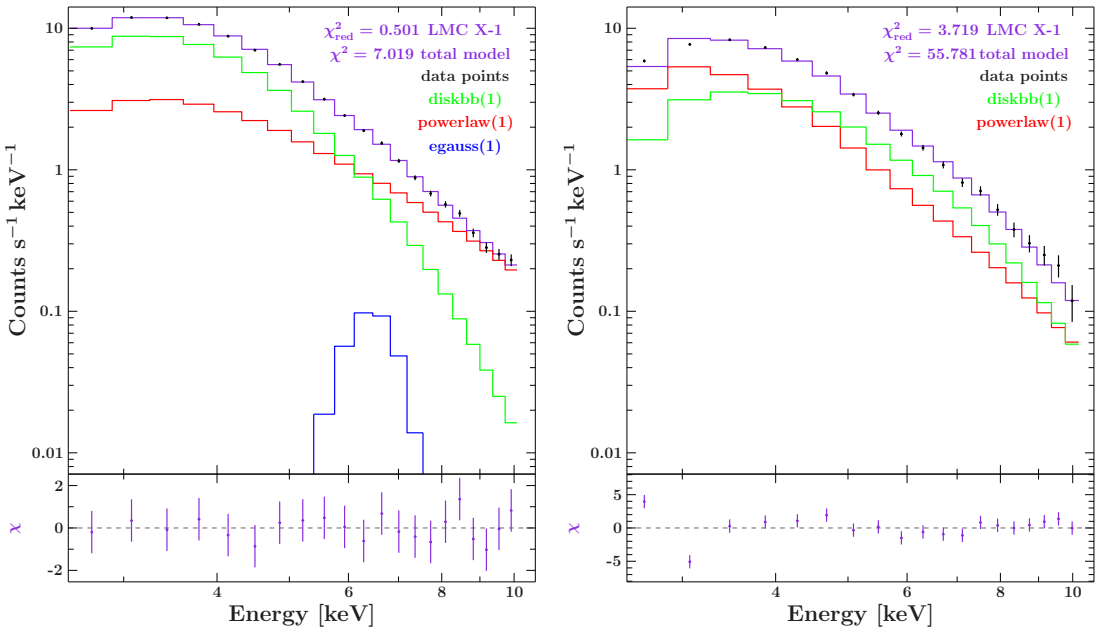

(a) 10250-01-03-00

(b) 93113-02-35-00

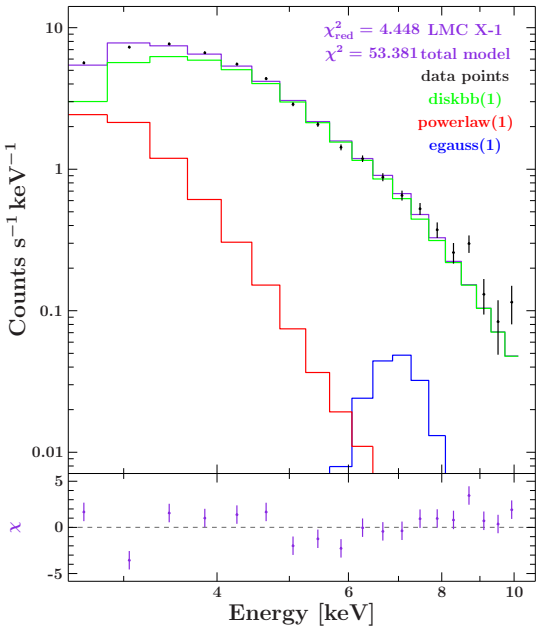

(c) 95113-02-52-00

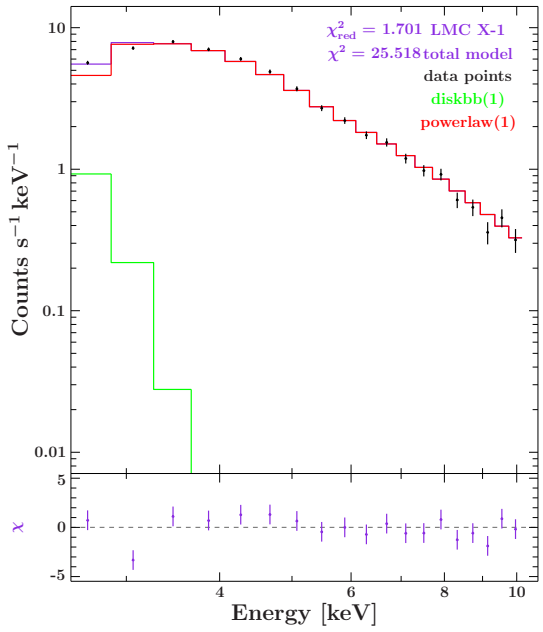

(d) 93113-02-38-10

Figure 10: Some spectral plots of LMC X-1 showing the data points, the total model and each separate model component, as well as the residuals of the total model and their respective χ^2_{red}-value; The code in the plot subcaption identifies which PCA observation the plot belongs to.

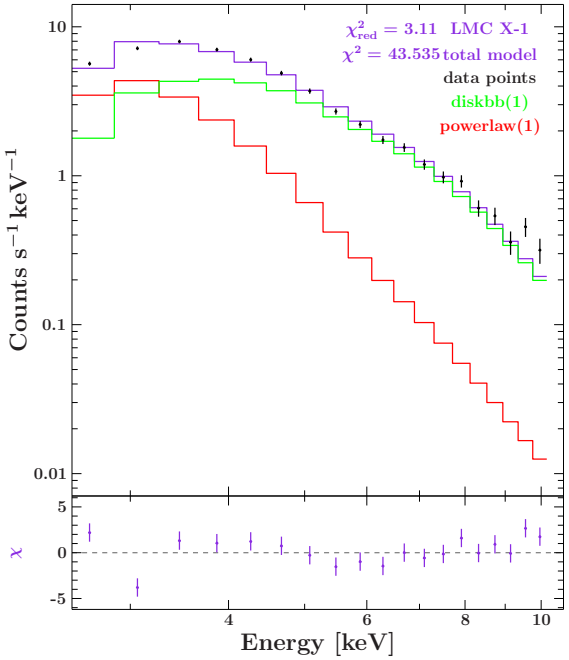

Figure 11: Adjusted fit of observation 93113-02-38-10.

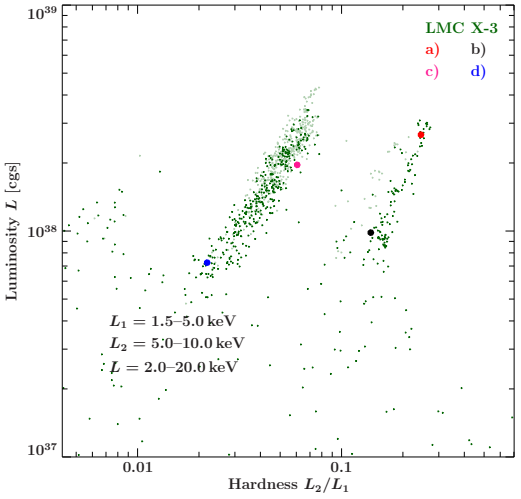

(a) HID of LMC X-3 with marked data points corresponding to spectral plots shown in Fig. 13; data points with χ_{reduced} < 3.5 shown in a lighter shade.

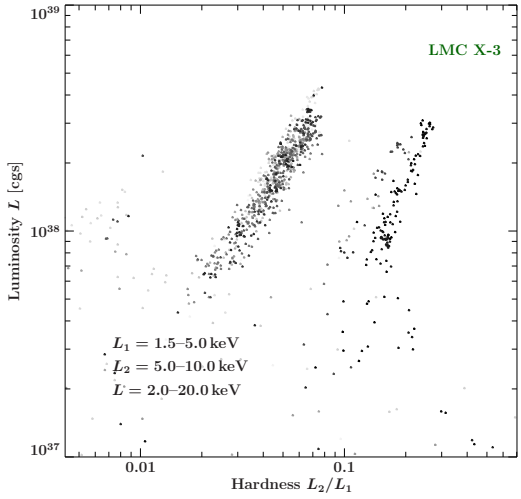

(b) LMC X-3 HID with a color gradient over the observation time; black=earlier observation (right diagonal), light grey=later observation (left diagonal).

Figure 12: Two different HIDs for LMC X-3.

in the HID diagram

Before continuing with the other two sources it should be noted that the fits of the two LMC sources are generally worse than the fits of GX 339–4 and Cygnus X-1, as can be seen in Fig. 8. This means the LMC-fits are generally less meaningful than the other fits. While one should keep this in mind it is also not really a big reason for concern, since the χ^2_{reducced}-values of the LMC-sources are still mostly bellow 5, they are just not as good as the χ^2_{reducced}-values of GX 339–4 and Cygnus X-1.

5.3 GX 339–4

After having shown the results for the two sources situated in the large magellanic cloud, the HIDs for the remaining sources will also be presented in the following. First up Fig. 14 shows the HID for GX 339–4, most remarkably here we can see the previously introduced q-shape of the HID for the first time. Not only does this HID show this shape but it also spans a much bigger luminosity range than the previous diagrams, ranging from $\approx 1 \times 10^{34}$–$1 \times 10^{38}\,\mathrm{erg\,s^{-1}}$. In addition to the big luminosity range this diagram also shows a comparably big hardness range (note the logarithmic axes of the HIDs), which means the spectral shape of GX 339–4 will also drastically change over time. Similar to LMC X-3 and LMC X-1, GX 339–4 also has a diagonal and a horizontal part in its HID, but unlike the other two sources GX 339–4 also has a big vertical part in its HID, spanning the entire luminosity range. This means the Luminosity of GX 339–4 varies extremely over time. Again I marked a few data points in the HID, each corresponding to a spectral plot showing the model and its component in figures 15a-15f. Starting on the bottom right of Fig. 14 and anti-clockwise making our way around the Q-diagram we first see a very low count rate in Fig. 15a. Here the data is almost indistinguishable from background noise, especially at energies above 10 keV. But despite the low count rate it is still possible to make out an emission line at around 7 keV. This is also what we see in most fits for this source, almost all best fits for each observation include this emission line and use the broken power law model instead of the normal power law model. Also here the power law model component is more dominant than the disk black body component, which was not the case for either of the LMC sources.

Following the HID anti-clockwise we reach the observation corresponding to Fig. 15b. Since we moved upwards in the HID the luminosity and thus also the overall count rate went up, Here again the broken power law model component is stronger than the disk black body part, this is also not surprising since here we are still in the hard state of GX 339–4. Also with the source now being more luminous overall, the emission line component also gets stronger.

Moving on to figures 15c and 15d we again can see an increase in count rate, since we moved even further up in the HID. But the most drastic change in these two diagrams compared to the previous one can be seen in their disk black body components, now this component is far weaker than before and only contributes significantly at low energies.

Moving further along the Q-diagram to Fig. 15e this changes again, as the sources enters its soft state. Here the disk black body component significantly surpasses the power law at low energies, while still being rather weak at high energies, this results in a extremely

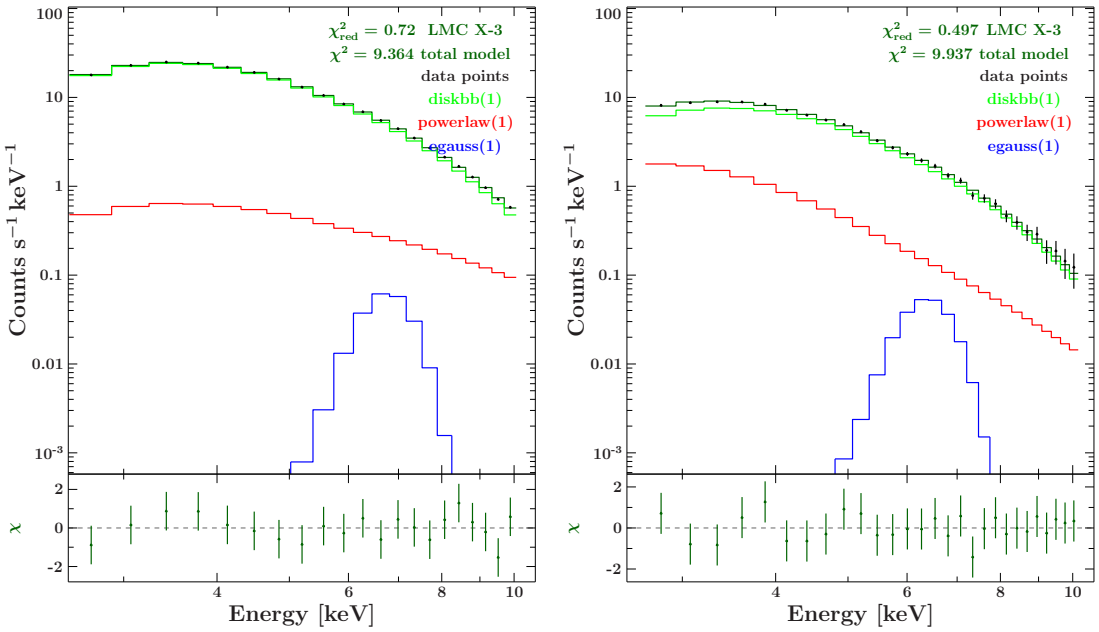

(a) 20188-02-01-010

(b) 10252-01-71-00

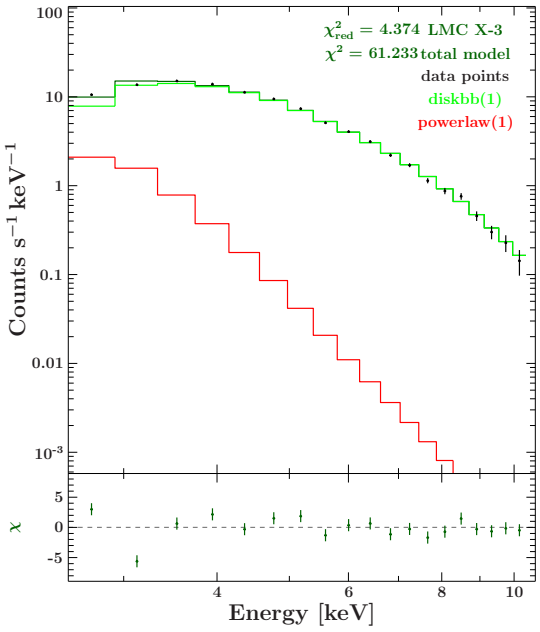

(c) 40067-01-06-01

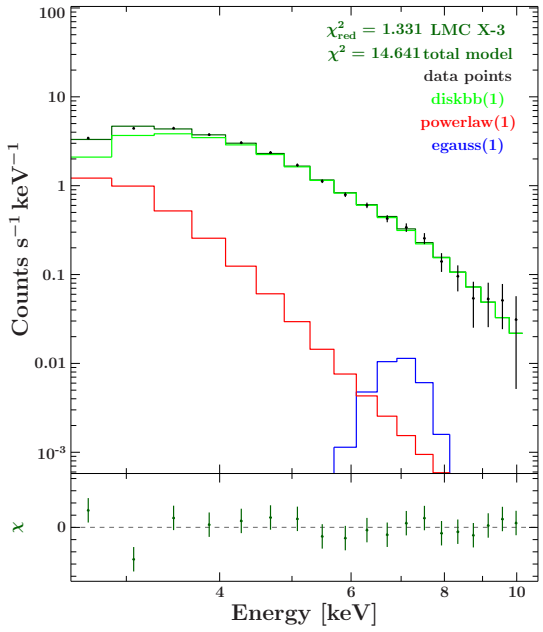

(d) 93113-01-49-00

Figure 13: Some spectral plots of LMC X-3 showing the data points, the total model and each separate model component, as well as the residuals of the total model and their respective χ^2_{red}-value; The code in the plot subcaption identifies which PCA observation the plot belongs to.

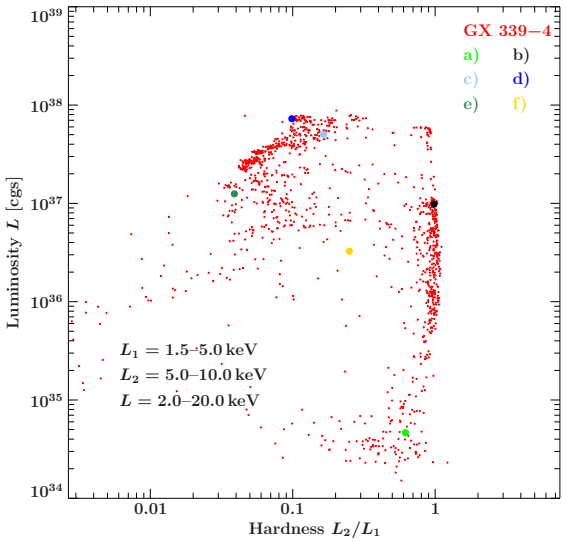

Figure 14: HID of GX 339−4 with marked data points corresponding to spectral plots shown in Fig. 15; data points with $\chi_{\mathrm{reduced}} < 3.5$ shown in a lighter shade.

steep spectrum. The state corresponding to this spectrum has already previously been analysed in Corbel et al. (2003).
In the last spectrum shown here (Fig. 15f) the source returns to having a weak black body component, here also the count rate dropped down, as we moved downwards in the HID. The broken power law component remains the dominant part of the spectrum.

5.4 Cygnus X-1

For the last source Fig. 16 again shows the corresponding HID with a few marked data points. When looking at this diagram it is again not quite as clear which part of the Q-diagram these data points inhabit. Nevertheless it is still possible to make out two main aspects of the q-shape in this HID. First the vertical part on the right hand side, followed by a more or less horizontal part stretching to the left. Here again the HID only stretches over a comparably small vertical luminosity range (2×10^{36}–$2 \times 10^{37}\,\mathrm{erg\,s^{-1}}$).
Starting from the bottom left we make out way anti-clockwise around the HID. As it already was the case for GX 339−4, the power law or in this case rather the broken power law component is more dominant than the disk black body component (see Fig. 17a). In addition to this we also see a distinct emission line between 6 keV and 8 keV as was also the case for GX 339−4. Moving on to the second marker in the HID (Fig. 17b) the situation barely changes to a now slightly higher count rate, which was to be expected, since we moved upwards in the HID. Coming now to the spectral plot corresponding to the yellow marker (Fig. 17c) we see a drastic change in the black body component. It massively loses strength at higher energies, but simultaneously gets stronger at low energies. This trend continues when going to Fig. 17d, here the total model is far steeper than at the beginning, mostly due to the strong black body component. The strong

black body component in figures 17c and 17d marks the soft state of Cygnus X-1. After this we move on to the lower left corner of its HID, where the count rate at low energies together with the black body component dropped back down, the broken power law component continues to be the dominant factor in this fit. Looking at the spectrum of

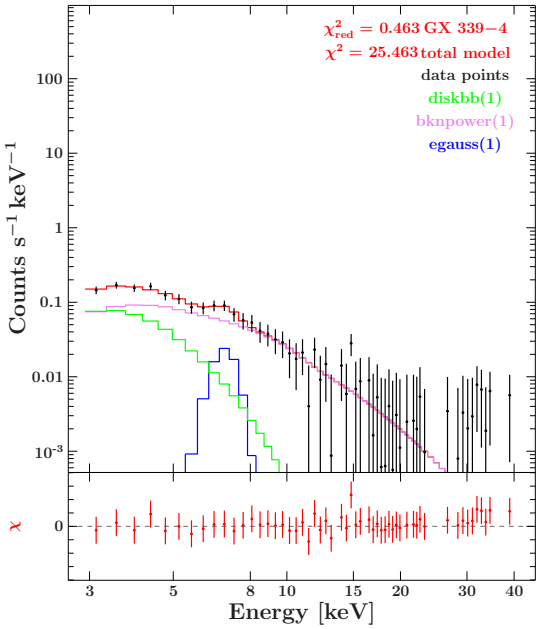

(a) 40108-03-01-00

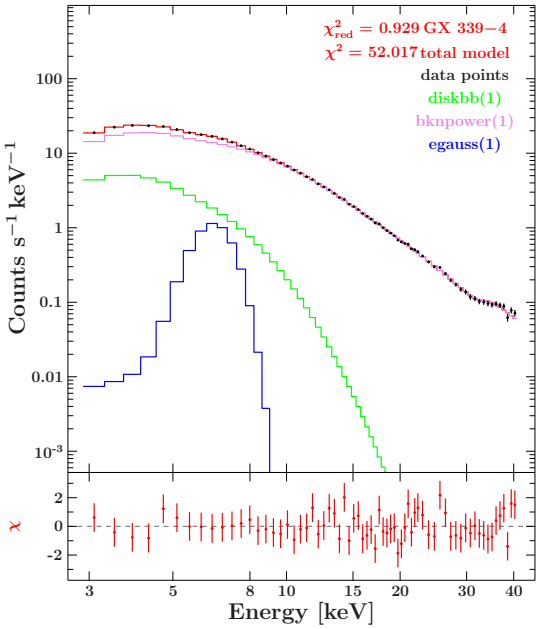

(b) 90118-01-07-00

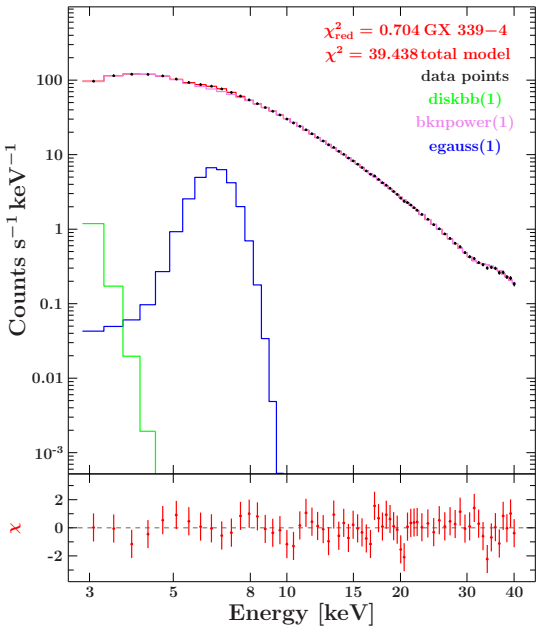

(c) 92035-01-01-02

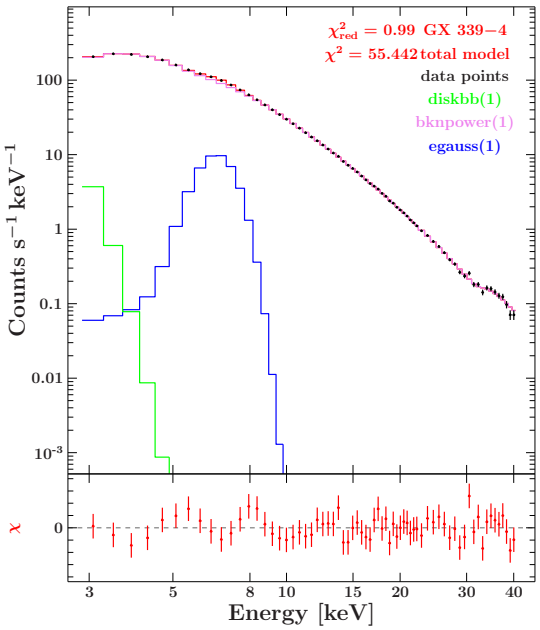

(d) 92035-01-03-02

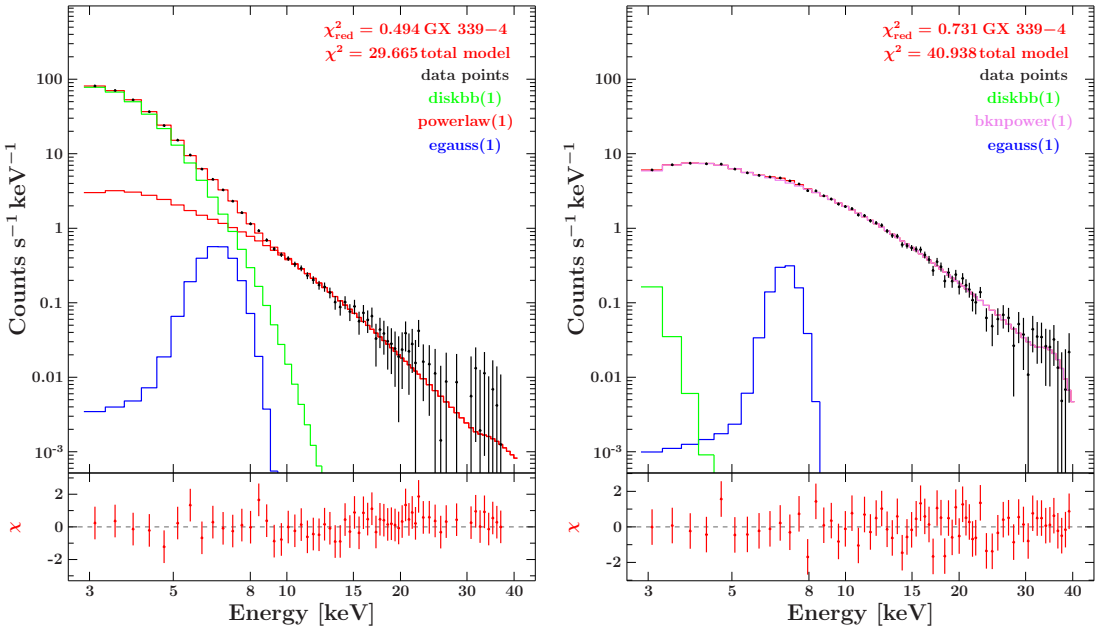

(e) 70109-01-35-00 (f) 92704-03-16-00

Figure 15: A few spectral plots of GX 339−4 showing the data points, the total model and each separate model component, as well as the residuals of the total model and their respective χ^2_{red}-value; The code in the plot subcaption identifies which PCA observation the plot belongs to.

the last marked data point, Fig. 17f, we do not see any change in the spectrum or the model components compared to the previous spectrum.

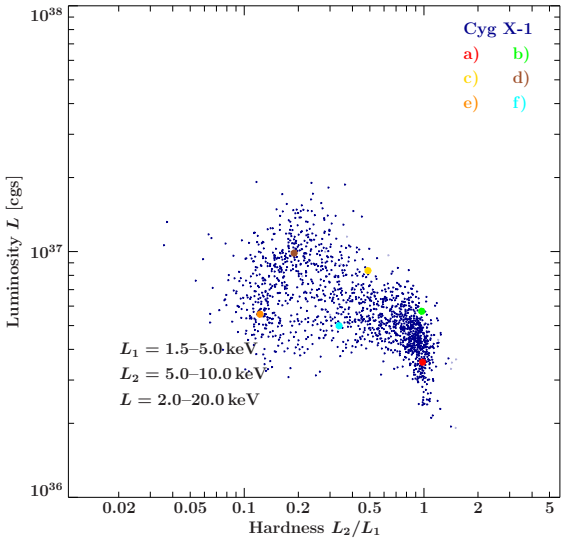

Figure 16: HID of Cygnus X-1 with marked data points corresponding to spectral plots shown in Fig. 17; data points with $\chi_{\text{reduced}} < 3.5$ shown in a lighter shade.

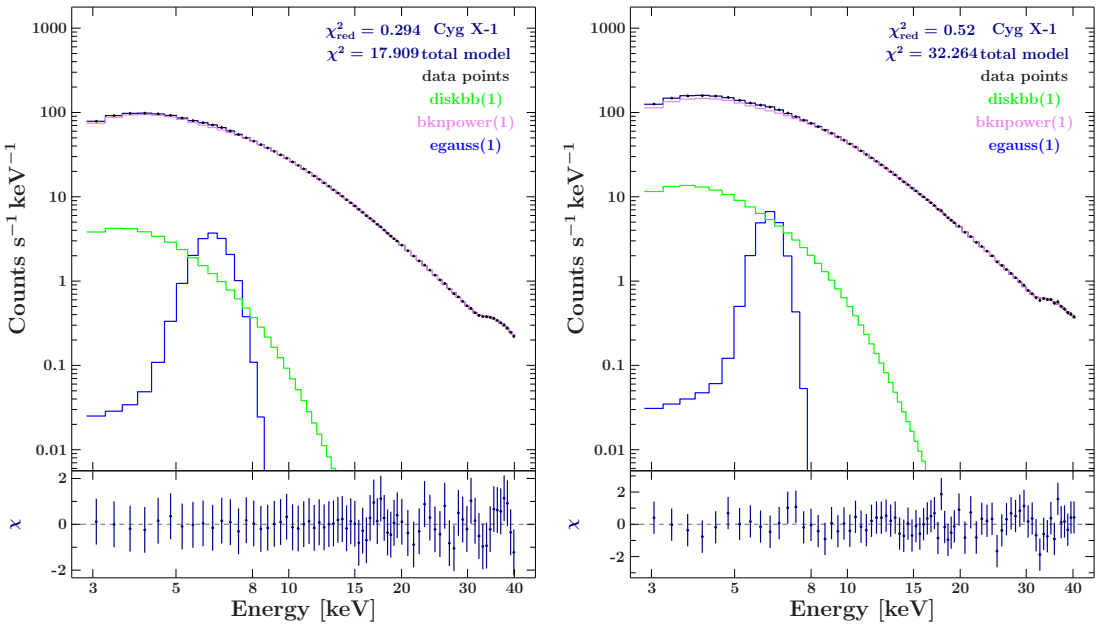

(a) 10239-01-01-00

(b) 30157-01-12-00

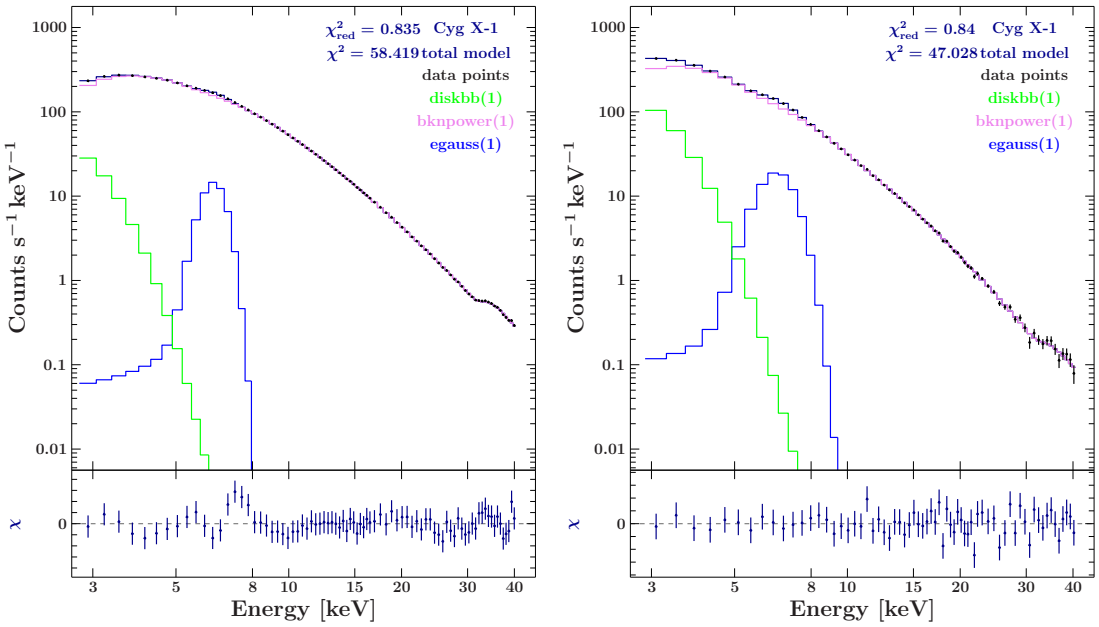

(c) 10238-01-04-00

(d) 80110-01-22-02

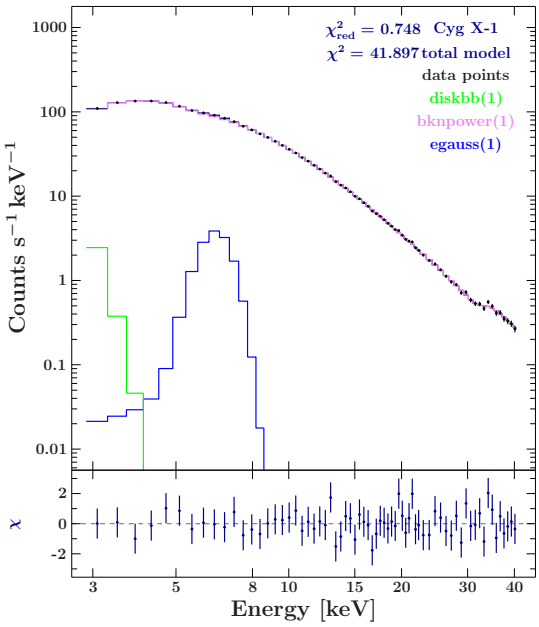

(e) 80110-01-30-02

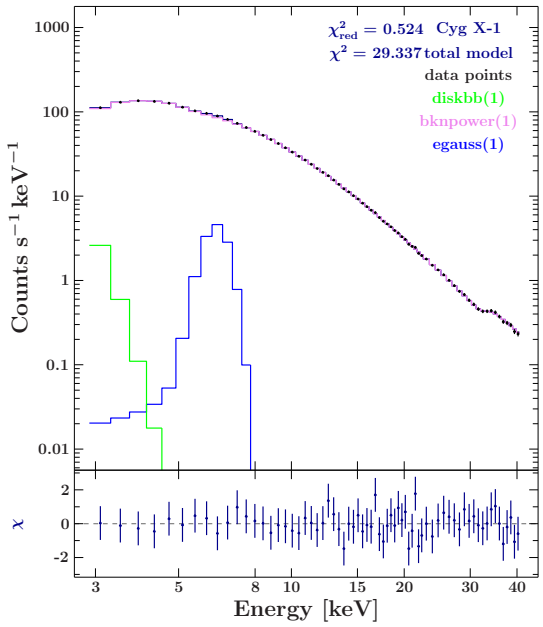

(f) 80110-01-08-00

Figure 17: Some spectral plots of Cygnus X-1 showing the data points, the total model and each separate model component, as well as the residuals of the total model and their respective χ^2_{red}-value; The code in the plot subcaption identifies which PCA observation the plot belongs to.

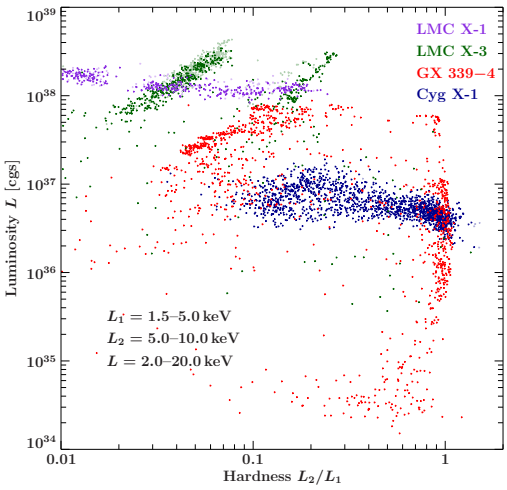

(a) Luminosity HID showing all four sources in one diagram.

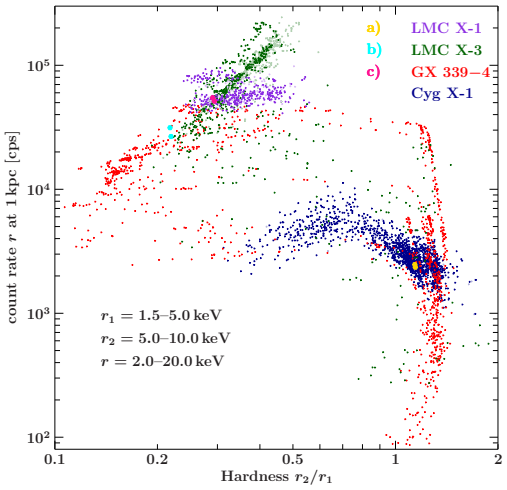

(b) Combined HID using the rate at 1 kpc on the y-axis (the source is calculated to be only 1 kpc away from the observer); example data points of overlapping regions marked in yellow, cyan, and pink respectively.

Figure 18: Combined HIDs of all four sources.

5.5 Combined HID

Finally to compare these four sources and to better understand which part in the q-shaped HID they occupy, Figs. 18a and 18b show all sources in one combined HID with the luminosity and the rate at 1 kpc on their respective y-axes. The second of these plots was done to be able to more easily compare the sources, as for this plot the difference in the distance to the objects not longer plays a role. As is clearly visible from these figures, GX 339–4 covers almost the complete range of the q-shape. Therefore the drastic changes in the spectrum of GX 339–4 are not surprising. The remaining sources on the other hand each only fill part of the q-shape. Cygnus X-1 remains on the right side of the lower horizontal branch during all observations, this explains why the (broken) power law component is always stronger than the disk black body part, as the source resides in a overall hard state for the majority of the observations. (Although Cygnus X-1 has both a harder and a softer state, every state of Cygnus X-1 would be classified as hard in the context of the combined HID.) Only few data points show the same hardness ratio as the majority of data points from the two LMC sources. This is especially evident in Fig. 18b, where the rate at a distance of 1 kpc is used instead of the luminosity.
Considering the positioning of the two LMC sources in Fig. 18a and 18b it is clear why the disk component usually contributes more than the power law model component. The LMC sources are both situated on the left side of the HID, therefore one also expects them to be in a soft state for most of the time.
To finish this section I also want to show a quick check for whether the HID can actually

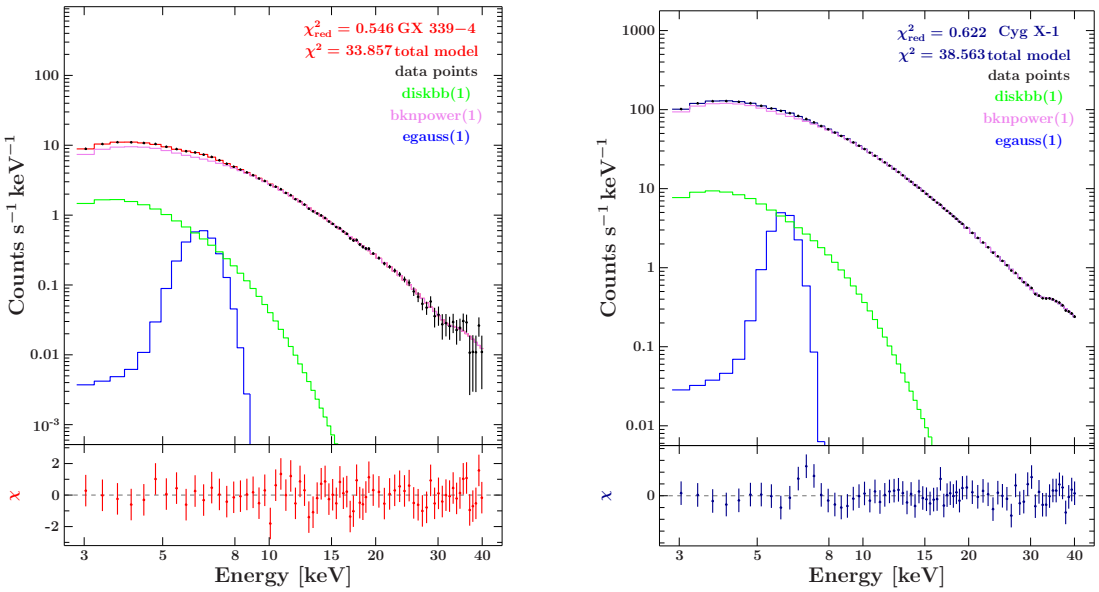

(a) 40108-01-04-00 (b) 30162-01-03-00

Figure 19: Spectra comparing the hard state of GX 339−4 and Cygnus X-1.

reflect general behavior of black hole binaries. For this I chose a few data points in Fig. 18b from regions where the point clouds of two sources overlap. A HID with these marked data points can be seen in Fig. 18b, each colored set of data points in this figure corresponds to one overlapping region and to two model component plots in Fig. 19, 20 and 21 respectively. It was necessary to mark these points in the rate-HID instead of the luminosity-HID, as the former puts all sources on more equal footing by showing the rate of each source at a distance of 1 keV, this two compare spectra that come from similar regions of this figure. Starting with Fig. 19 it is clear that both sources have a very similar spectral shape. Furthermore the model components of both sources also behave the same, with the (broken) power law being the more dominant part and the black body part mainly contributing at low energies, falling off towards zero at around 15 keV. But despite their similarities these diagrams also show some differences, namely their count rates and their gaussian emission line component. The former can easily be explained by the close proximity of Cygnus X-1 (see section 3). The different shapes seen in the two emission lines might be caused by different element compositions in the two sources accretion disks. The model component plots corresponding to the other two overlap regions each share similar qualities. This can be seen in figures 20 and 21. For Fig. 20b I adjusted the x-axis to only range up to 10 keV, instead of the usual 40 keV for this source, to make the two plots easier to compare. As shown in Fig. 20 both sources have a very pronounced black body component as well as a rather flat but less strong (broken) power law part that becomes stronger than the disk black body component only at energies $\gtrsim$ 8 keV. Again both the shape of the gaussian emission line and the overall count rate of

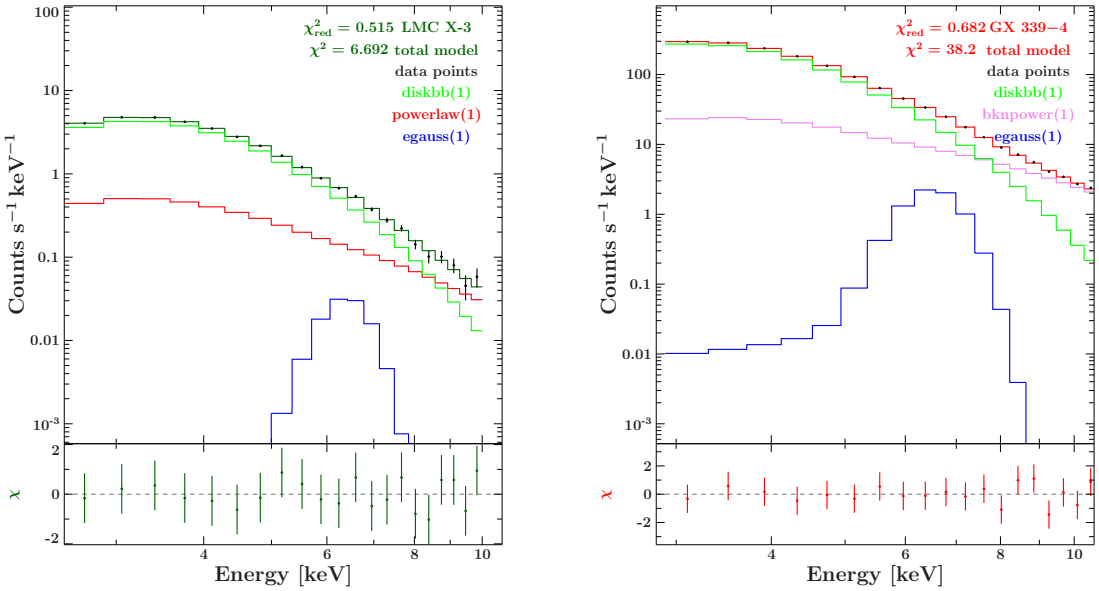

(a) 20189-01-01-01 (b) 70110-01-23-00

Figure 20: Spectra comparing the soft state of LMC X-3 and GX 339−4.

these two sources differ for the same reasons given before. Looking at the plots shown in Fig. 21 one has to admit that the differences between the spectra of the two sources LMC X-1 and LMC X-3 are bigger than they were in the previous comparisons. LMC X-1 appears to have an overall steeper spectrum than LMC X-3, both in its disk as well as in its power law component. There are multiple reasons that could cause these differences like the vastly different N_{H}-values of theses sources ($1.0\times10^{22}\,\mathrm{cm}^{-2} \leq N_{\mathrm{H}} \leq 1.3\times10^{22}\,\mathrm{cm}^{-2}$ for LMC X-1 and $\leq 0.08\times10^{22}\,\mathrm{cm}^{-2}$ for LMC X-3) or the difference in the masses of their compact objects. But since this is not the main focus of this work, this will not be investigated any further. The main point of this check was to verify that the sources do not behave completely different when being in similar parts of the HID, which they do not. Therefore this confirms that at least for these sources it is justified to use HIDs to analyse their variability behavior. Remember if the sources would have shown sufficiently different spectral shapes in overlapping regions of the HID this would mean HIDs are not a good way of finding a general behavior of black hole binaries. This could be the case for some other source that is not included in this work, but at this point this can neither be confirmed nor falsified.

In addition to the combined HID shown in Fig. 18 I also plotted the same HID with a color grading showing the behavior of some parameters. This is shown in Fig. 22, here the shape of the data points corresponds to each source. The color in this plot indicates the value of the parameter shown on the label of the color-bar of each plot, blue colors correspond to a low value and red colors to a higher value. Each of these plots uses the rate at a distance of 1 kpc for the Intensity to make the data points of the

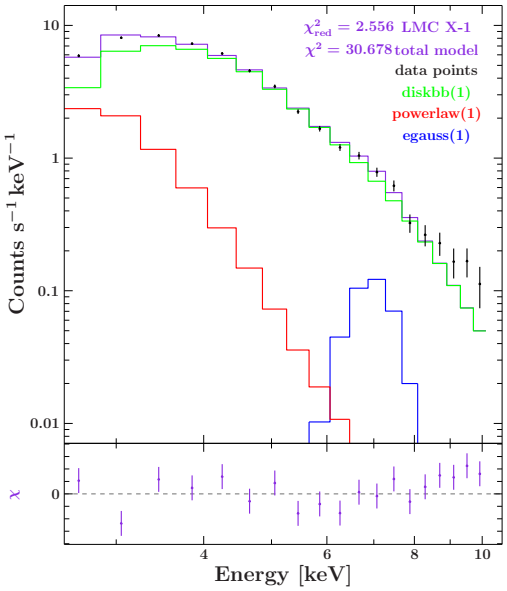

(a) 95113-02-79-00

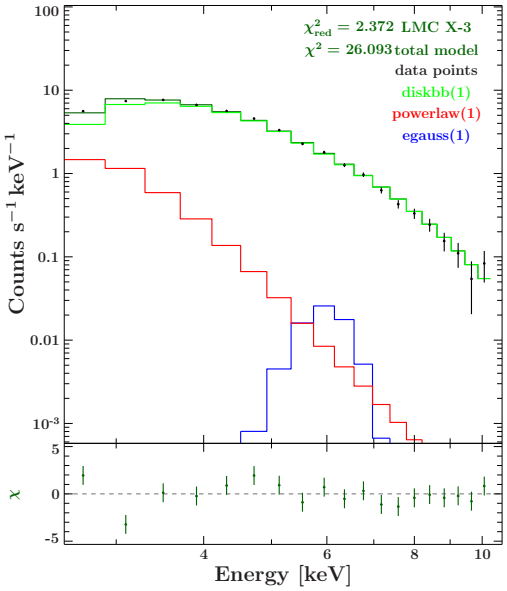

(b) 80103-01-06-01

Figure 21: Spectra comparing the soft state of LMC X-1 and LMC X-3.

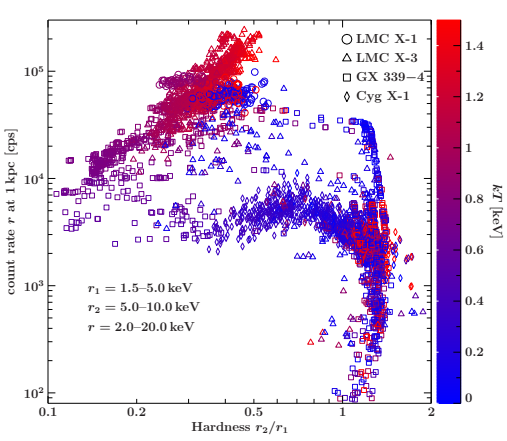

(a) HID showing the behavior of the temperature parameter of the disk black body model.

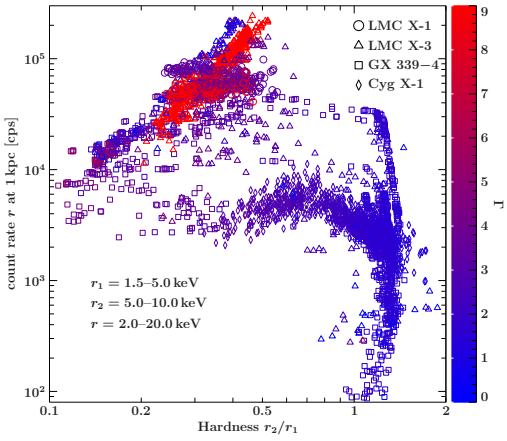

(b) HID showing the behavior of the photon index, using Γ_1 as the photon index for model containing a broken power law.

Figure 22: Combined HIDs showing the behavior of two parameters

different sources as comparable as possible. As can be seen in Fig. 22a and 22b both LMC sources show a high disk temperature and high photon index. This high photon index corresponds to a steep power law component, which is also what we previously saw in the model component plots (Fig. 10 and 13). A similar behavior can be seen in Fig. 22a, the higher one moves up along the left diagonal of the HID, the higher the disk temperature becomes. Also observations corresponding to points further left in the HID seem to correspond to higher temperatures, which is in accordance with the definitions of soft and hard states. The red data points seen in Fig. 22a likely come from fits that ended up in the wrong minimum during fitting, this would have to be examined more thoroughly in a future analysis.
Both of these HIDs show behavior in accordance with the way soft and hard states were defined at the beginning.

5.6 Validation of previous results

In addition to these HIDs the analysis of the four sources also led to the confirmation of two previous results. First a result from Hanke et al. (2010) about the N_{H}-value of LMC X-1 was validated. Furthermore I was able to recreate two correlations results for parameters of the broken power law and high energy cutoff models for Cygnus X-1. This was previously done in Grinberg (2013).

N_{H}-value confirmation:
In Hanke et al. (2010) it was found that the hydrogen column density of LMC X-1 lies in the range of 1.0×10^{22}–$1.3 \times 10^{22}\,\mathrm{cm}^{-2}$. To test this first I fixed the N_{H}-value at various values inside and outside the aforementioned range, then I fit the model to the data and finally compared the results from these fits. The comparison between these fits was done separately for each model and used a fit with a N_{H}-value of $1.15 \times 10^{22}\,\mathrm{cm}^{-2}$ as a baseline. One result of this comparison can be seen in figures 23a and 23b. If the models were independent of the N_{H}-value these plots would only show a straight line through the origin. Offsets or other differing behavior from this line indicate that the disk temperature is in some way dependent on the N_{H}-value. As shown in from these plots varying the N_{H}-value within the range found in Hanke et al. (2010) results in three parallel lines of disk temperature values, this means that the change in N_{H}-value only changes the disk temperature behavior by a slight offset and not in any other way like slope or curvature of these point cloud lines. This changes when fixing the N_{H}-value outside of the found range, doing this firstly results in a significantly bigger offset as well as in a change in slope. An N_{H}-value below the found range results in a steep slope, whereas a higher N_{H}-value gives a more flat line compared to N_{H}-values within the range of 1.0×10^{22}–$1 \times 10^{22}\,\mathrm{cm}^{-2}$. This confirms the result found in Hanke et al. (2010) Although there is plenty of more to be discussed about this aspect of LMC X-1, it will not be further explored within this thesis, as this would surpass the scope of this work.

Validation of parameter correlation results:
The first correlation validated here is the one between the two photon indices Γ_2 and

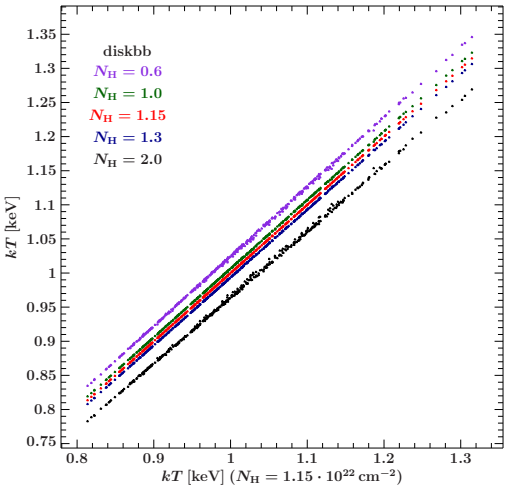

(a) Disk temperature comparison plot using `diskbb` as a fit model.

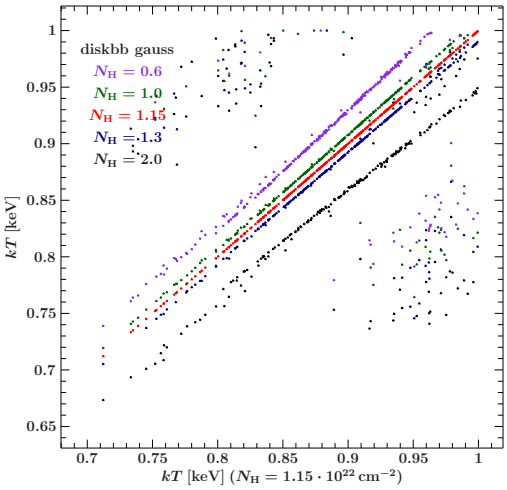

(b) Disk temperature comparison plot using `diskbb` and `egauss` as fit model components.

Figure 23: Each dot in this plot corresponds to an observation; it shows parameter value of the disk temperature of each observation for two models, with the value for an N_H-value of 1.15×10^{22} cm^{-2} on the x-axis and the temperature values for various other N_H-values on the y-axis.

Γ_1 of the broken power law model. This is shown in Fig. 24a, as is visible from this figure the two parameters are strongly correlated. The same result was previously found by Grinberg (2013) and in the there referenced publication by Wilms, J. et al. (2006). Figure 24b shows the second correlation between parameters of the broken power law, it is between the second photon index Γ_2 and the break energy E_{Break}. Again the figure shows a very similar correlation to the one found by Grinberg (2013). Important to note is the fact that in my work I only used PCA data, wheres in the referenced thesis (Grinberg 2013) both PCA and HEXTE data were used, HEXTE being another detector aboard the RXTE satellite. As mentioned in Grinberg (2013) the parameter correlations of the high energy cut-off model solely using PCA data deviates visibly from the one using both PCA and HEXTE data. Therefore no correlation plots for this model are shown in this work.
In the following final part of this thesis a brief outlook of what could be improved or expanded upon will be given.

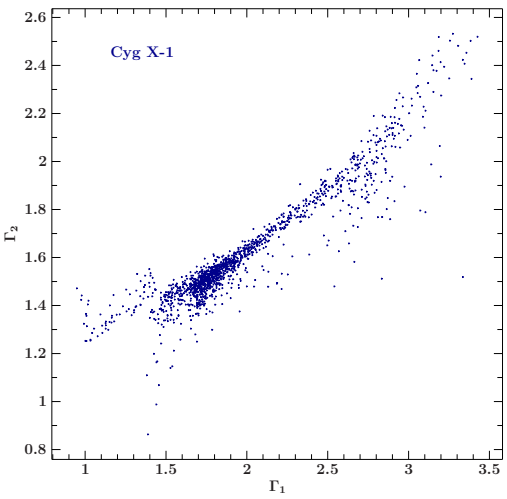

(a) Parameter correlations between the two photon indices of the broken power law model used for Cygnus X-1.

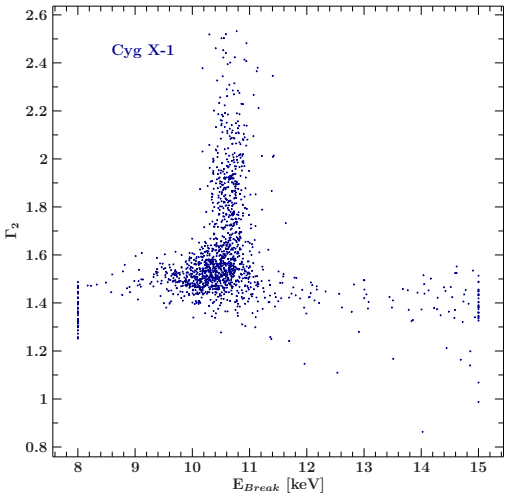

(b) Correlation between Γ_2 and the break energy E_{Break}.

Figure 24: Correlation plots for the parameters of the broken power law model used for Cygnus X-1.

6 Outlook

After having presented the results of this analysis I want to give a brief overview of what could be added to this analysis, but also what could be improved about it in the future. First one could improve upon the currently used empirical models and apply other ones, such as `cutoffpl`, which is a power law with a high energy exponential roll-off, described by the following formula:

$$A(E) = K \cdot E^{-\Gamma} \cdot \exp(-E/E_{\text{fold}}) \tag{6.1}$$

where E is the energy used as the input variable , Γ the power law photon index and E_{fold} the folding energy of the exponential roll-off. Another example is the `simpl`-model (Steiner et al. 2009). Applying more empirical models to the data would be an easy way of potentially improving the fits and making sure that the empirical models really describe the spectral behavior, as there might be aspects of the spectra that are not correctly described by the currently used model. This might especially be the case for the two LMC sources and could maybe also explain their currently less than ideal χ^2_{red}-values (see Fig. 8)
In addition to using more empirical models one would also have to use physical models for a further analysis of the objects, like for example `relxill` (García et al. 2014; Dauser et al. 2014). Also using and comparing different physical models would allow to determine which physical model is the most general one and which ones are equivalent. This step should definitely be done in the future as this thesis is meant as part of the groundwork

for this endeavour.
Of course comparing physical models with each other would be almost meaningless if they are not compared to the previously discussed empirical ones. This comparison is necessary to make sure the physical models actually describe the data, as they have to match the result from the empirical ones.
Lastly to improve the current status of this work one could add more X-ray sources to the analysis to see if the previously fitted models are still able to describe the data of new sources. If a physical model is no longer able to describe the source in agreement with the best fitting empirical model one should reject this physical model and use a model that can be applied to all sources. Repeating this process one would hopefully be able to sift out a general model applicable to all X-ray binaries containing a black hole as the compact object. Furthermore one might realise that there are multiple models equally good at describing these kind of objects and that it might currently be impossible to determine which one is generally speaking better.

7 Acknowlegements

Before finishing this thesis I want to thank a few people. First I want to say thank you to my supervisor Prof. Dr. Jörn Wilms for always giving me some good pieces of advice, whenever I was stuck on a problem or did not know how to proceed with the analysis. But not only did he advise me during my project, but at the beginning of the project he also provided me with a few very helpful ISIS-scripts to get me started with the thesis work. In addition to these ISIS-scripts he also provided me with already extracted data files, so I was able to start with fitting and analysing the data right away.
Also I want to thank two more people from the Remeis observatory: Dr. Thomas Dauser and Amy Joyce. Although they did not advise me for most parts of this project, they helped me greatly during a previous research project at the observatory, teaching me how to uses the necessary software tools, which I could again apply during the work for this bachelors thesis. Finally I want to again thank Jörn Wilms and Thomas Dauser for proof reading the first draft of this thesis.

8 References

Barr, P., White, N. E., & Page, C. 1985, Space Sci. Rev., 40, 383

Böck, M., Grinberg, V., Pottschmidt, K., et al. 2011, A&A, 533, A8

Bolton, C. T. 1972, Nature, 235, 271

Carroll, B. W. & Ostlie, D. A. 2017, An Introduction to Modern Astrophysics, 2nd edn. (Cambridge University Press)

Corbel, S., Nowak, M. A., Fender, R. P., Tzioumis, A. K., & Markoff, S. 2003, A&A, 400, 1007

Dauser, T., Garcia, J., Parker, M. L., Fabian, A. C., & Wilms, J. 2014, MNRAS, 444, L100 ff.

Frnka, R. 2010, The circular restricted three-body problem

García, J., Dauser, T., Lohfink, A., et al. 2014, ApJ, 782, 76

Grinberg, V. 2013, PhD thesis, Friedrich-Alexander-University Erlangen-Nürnberg

Hanke, M., Wilms, J., Nowak, M. A., Barragán, L., & Schulz, N. S. 2010, A&A, 509, L8

Hilditch, R. W. 2001, An Introduction to Close Binary Stars

Houck, J. C. & Denicola, L. A. 2000, in Astron. Soc. Pacific Conf. Ser., Vol. 216, Astronomical Data Analysis Software and Systems IX, ed. N. Manset, C. Veillet, & D. Crabtree, 591

Hyde, E. A., Russell, D. M., Ritter, A., et al. 2017, PASP, 129, 094201

Hynes, R. I., Steeghs, D., Casares, J., Charles, P. A., & O'Brien, K. 2004, ApJ, 609, 317

Jahoda, K., Markwardt, C. B., Radeva, Y., et al. 2006, ApJS, 163, 401

Jahoda, K., Swank, J. H., Giles, A. B., et al. 1996, in Society of Photo-Optical Instrumentation Engineers (SPIE) Conference Series, Vol. 2808, EUV, X-Ray, and Gamma-Ray Instrumentation for Astronomy VII, ed. O. H. Siegmund & M. A. Gummin, 59–70

Kong, A. K. H., Charles, P. A., Kuulkers, E., & Kitamoto, S. 2002, MNRAS, 329, 588

Lubow, S. H. & Shu, F. H. 1975, ApJ, 198, 383

Makishima, K., Maejima, Y., Mitsuda, K., et al. 1986, ApJ, 308, 635

Miller-Jones, J. C. A., Bahramian, A., Orosz, J. A., et al. 2021, Sience, 371, 1046

Mitsuda, K., Inoue, H., Koyama, K., et al. 1984, PASJ, 36, 741

Mondal, S., Adhikari, T. P., & Singh, C. B. 2021, MNRAS, 505, 1071

Mondal, S., Debnath, D., & Chakrabarti, S. K. 2014, ApJ, 786, 4

Page, M. J., Soria, R., Wu, K., et al. 2003, MNRAS, 345, 639

Park, T., Kashyap, V. L., Siemiginowska, A., et al. 2006, ApJ, 652, 610

Pietrzyński, G., Graczyk, D., Gallenne, A., et al. 2019, Nature, 567, 200

Steiner, J. F., McClintock, J. E., Orosz, J. A., et al. 2014, ApJ, 783, 101

Steiner, J. F., Narayan, R., McClintock, J. E., & Ebisawa, K. 2009, PASP, 121, 1279

Sunyaev, R. A. & Titarchuk, L. G. 1985, A&A, 143, 374

Tananbaum, H., Gursky, H., Kellogg, E., Giacconi, R., & Jones, C. 1972, ApJ, 177, L5

Tetarenko, B. E., Sivakoff, G. R., Heinke, C. O., & Gladstone, J. C. 2016, ApJS, 222, 15

Wilms, J. 2022, Lecture notes in X-Ray Astronomy II

Wilms, J., Allen, A., & McCray, R. 2000, ApJ, 542, 914

Wilms, J., Nowak, M. A., Pottschmidt, K., et al. 2001, MNRAS, 320, 327

Wilms, J., Nowak, M. A., Pottschmidt, K., Pooley, G. G., & Fritz, S. 2006, A&A, 447, 245

Xiang, J., Lee, J. C., Nowak, M. A., & Wilms, J. 2011, ApJ, 738, 78

Zdziarski, A. A., Gierlinski, M., Mikolajewska, J., et al. 2004, MNRAS, 351, 791

9 Eigenständigkeitserklärung

Hiermit bestätige ich, dass die hier vorliegende Arbeit von mir selbst verfasst wurde. Dabei wurden nur die angegebenen Quellen und Hilfsmittel verwendet, ebenfalls wurde die vorgegebene Laufzeit des Projekts eingehalten. Des Weiteren bestätige ich, dass die Arbeit meines Wissens nach nicht in wesentlichen Teilen mit einer anderen Arbeit übereinstimmt, welche bereits dieser oder einer anderen Prüfungsbehörde vorgelegt wurde.

David Horn

Ort, Datum